

A Gift from the Integration of Discriminative and Diffusion-based Generative Learning: Boundary Refinement Remote Sensing Semantic Segmentation

Hao Wang, Keyan Hu, Xin Guo, Haifeng Li, and Chao Tao,

Abstract—Remote sensing semantic segmentation must address both what the ground objects are within an image and where they are located. Consequently, segmentation models must ensure not only the semantic correctness of large-scale patches (low-frequency information) but also the precise localization of boundaries between patches (high-frequency information). However, most existing approaches rely heavily on discriminative learning, which excels at capturing low-frequency features, while overlooking its inherent limitations in learning high-frequency features for semantic segmentation. Recent studies have revealed that diffusion generative models excel at generating high-frequency details. Our theoretical analysis confirms that the diffusion denoising process significantly enhances the model’s ability to learn high-frequency features; however, we also observe that these models exhibit insufficient semantic inference for low-frequency features when guided solely by the original image. Therefore, we integrate the strengths of both discriminative and generative learning, proposing the Integration of Discriminative and Diffusion-based Generative Learning for Boundary Refinement (IDGBR) framework. The framework first generates a coarse segmentation map using a discriminative backbone model. This map and the original image are fed into a conditioning guidance network to jointly learn a guidance representation subsequently leveraged by an iterative denoising diffusion process refining the coarse segmentation. Extensive experiments across five remote sensing semantic segmentation datasets (binary and multi-class segmentation) confirm our framework’s capability of consistent boundary refinement for coarse results from diverse discriminative architectures. The source code will be available at <https://github.com/KeyanHu-git/IDGBR>.

Index Terms—Remote sensing semantic segmentation, boundary refinement, diffusion model, discriminative model, coarse segmentation refinement

I. INTRODUCTION

SEMANTIC segmentation aims to classify each pixel in an image, thereby partitioning the image into multiple regions with specific semantic meanings. In remote sensing, semantic segmentation is also known as land use or land cover classification, representing a fundamental task in remote sensing image analysis. Semantic segmentation of remote sensing images provides crucial support for numerous remote sensing

applications, including geographic information updates, environmental monitoring, urban planning, among others.

In recent years, with the development of deep learning technology, semantic segmentation methods utilizing deep learning for remote sensing images have overcome the performance bottlenecks of traditional pixel-oriented or object-oriented segmentation approaches [1], [2], [3]. Although these methods have significantly improved segmentation performance, they often fail to produce satisfactory boundary segmentation results [4]. Most studies attribute the difficulty of boundary region segmentation to the fact that segmentation models rely on large-scale features to capture contextual information from spatial neighborhoods [5], [6]. Compared to local features, large-scale features indeed provide richer semantic information. However, large-scale features are typically obtained from low-resolution feature maps, large receptive fields, long-range pixel relationships, or global pixel associations, thereby sacrificing local detail information. To address this issue, many studies have attempted to combine contextual semantic feature learning with boundary-sensitive local feature learning. Bertasius et al. [7] enhanced the model’s boundary localization awareness by jointly optimizing pixel-wise affinity loss and semantic segmentation loss. Ding et al. [8] introduced an additional boundary category to be optimized along with semantic categories, and utilized a directed acyclic graph structure to use the learned boundaries to isolate contextual information propagation between different regions. Wang et al. [9] designed a boundary-guided multi-scale feature fusion module to enhance boundary information preservation in multi-scale features. Considering the variability of boundary pixels between different categories, Wu et al. [10] pulled each boundary pixel closer to its nearest local category center while pushing it away from surrounding categories.

However, existing studies primarily focus on enhancing intra-class similarity and inter-class separability in boundary regions under discriminative classification strategies, without adequately addressing the negative effects of discriminative learning on boundary segmentation. Boundaries represent local transitions between adjacent regions in the spatial domain. From a signal frequency perspective, boundaries correspond to high-frequency components in the frequency domain. Studies have shown that Convolutional Neural Networks (CNNs) can capture high-frequency components in image features [11]. However, discriminative classification tends to make CNNs prioritize learning low-frequency components while suppressing high-frequency ones [12]. This leads to insufficient feature

Hao Wang is with the School of Geosciences and Info-Physics, Central South University, Changsha 410083, China, and also with the College of Computer Science, Inner Mongolia University, Hohhot 010021, China.

Keyan Hu, Xin Guo, Haifeng Li, and Chao Tao are with the School of Geosciences and Info-Physics, Central South University, Changsha 410083, China.

Corresponding author: Chao Tao (email: kingtaochao@csu.edu.cn).

learning for boundary pixels, thereby increasing the likelihood of misclassification. From a probability theory perspective, discriminative classification directly learns the posterior distribution, disregarding the inherent characteristics of the data itself and focusing solely on minimizing overall classification errors in the pixel space for given input data [13]. Due to the small proportion of boundary pixels in the pixel space, errors in boundary pixel classification are often overlooked or suppressed during the discriminative learning process [14].

Unlike discriminative learning, generative learning aims to produce high-fidelity samples by modeling the joint distribution of input data [13]. Therefore, theoretically, generative learning needs to accurately model both low-frequency content structures and high-frequency edge details in images, without neglecting or suppressing the learning of high-frequency components as discriminative learning does. However, for generative models such as VAEs and GANs, learning the distribution of high-frequency components remains challenging [15]. In recent years, diffusion probabilistic models have achieved breakthrough progress in generative tasks by gradually adding noise to data and learning the reverse denoising process, thereby generating high-quality samples [16], [17], [18]. In image generation tasks, studies have found that diffusion generative models enhance the learning of high-frequency components in images [19]. This paper also observes similar experimental phenomena in semantic segmentation tasks: by using remote sensing images as conditional information and applying diffusion noise training with Stable Diffusion [16] to segmentation label map encoded features, more realistic segmentation boundaries can be obtained. As shown in Fig. 1 (a), when we transform the segmentation maps generated by diffusion models into the frequency domain via Fourier transform, compared to discriminative models, diffusion generative models produce segmentation results in boundary regions that appear closer to the geometric contours of targets. However, from the perspective of overall segmentation metrics, there remains a significant gap in semantic reasoning accuracy between the segmentation results of diffusion generative models and discriminative models [20], as shown in Fig. 1 (b).

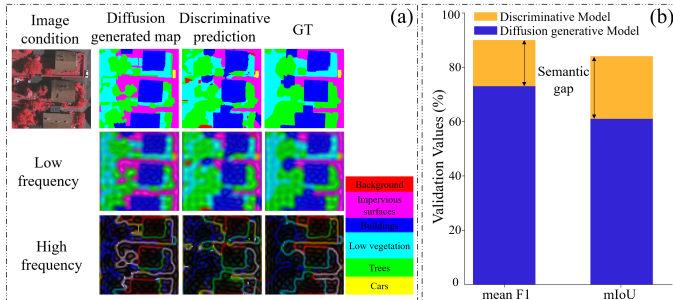


Fig. 1: Comparison between the diffusion generative model and the discriminative model on remote sensing image semantic segmentation tasks. (a) From the visualization results, the diffusion generative model produces segmentations that more closely adhere to the target boundaries; (b) From overall segmentation metrics, there exists a significant gap in semantic reasoning accuracy between the two model types.

In summary, discriminative learning excels at capturing low-frequency large-scale semantic features but struggles with accurately learn high-frequency boundary features; conversely, diffusion generative learning can effectively capture high-frequency boundary features but lacks accuracy in inferring semantic features. Based on the above analysis and observations, we propose the Integration of Discriminative and diffusion-based Generative learning for Boundary Refinement (IDGBR) framework, which includes a diffusion generative model, a discriminative model, and a conditional guidance network. First, to ensure semantic accuracy of the overall segmentation, IDGBR uses coarse segmentation results predicted by a discriminative model as semantic guidance conditions for diffusion generative learning. Although these coarse segmentation results have inaccurate boundary regions, they provide reliable semantic information for interior regions. Second, IDGBR learns joint guidance representations from coarse segmentation results and remote sensing images through a conditional guidance network, which are input to the diffusion generative model via residual connections, promoting more accurate inference of semantic features and boundary features by the generative model. Finally, we also use a simple regularization technique that explicitly aligns diffusion generative representations with joint guidance representations at intermediate network layers, greatly improving the training efficiency of diffusion generative semantic segmentation.

The main contributions of this paper are summarized as follows:

- We demonstrate the effectiveness of boundary segmentation from the perspective of diffusion generative learning. Compared to discriminative models, diffusion generative models can better capture high-frequency boundary features, enabling them to generate more refined segmentation boundaries in remote sensing image semantic segmentation tasks.
- We propose a remote sensing image semantic segmentation framework IDGBR for boundary refinement. IDGBR combines the advantages of discriminative learning and diffusion generative learning, learning joint guidance representations from coarse segmentation maps predicted by discriminative models and remote sensing images through a conditional guidance network, providing useful guidance for the diffusion generative model to learn semantic features and boundary features.
- We introduce a regularization technique to explicitly align diffusion generative representations with joint guidance representations, improving the training efficiency of diffusion generative semantic segmentation.
- We evaluate the effectiveness of our method across different remote sensing scenarios through extensive experiments. Results on five semantic segmentation datasets demonstrate that the proposed IDGBR achieves significant improvements in boundary region segmentation.

II. RELATED WORK

A. General Semantic Segmentation

Remote sensing semantic segmentation often faces challenges such as insufficient boundary refinement

[21],[22],[23],[24], semantic ambiguity [25], and missed segmentation of small-scale targets [6],[26],[27] due to large intra-class differences, low inter-class discrimination, and class imbalance in remote sensing features, as well as the large size, significant scale variations, and high scene complexity of remote sensing images. To address these issues, researchers have conducted a series of explorations.

CNNs represent the classical architecture in remote sensing semantic segmentation, with numerous research efforts building upon their strong local feature extraction capabilities to enhance the perception of multi-scale contextual information and boundary details[28], [29], [30]. Meanwhile, Transformers [31] have significantly enhanced the modeling of long-range dependencies in remote sensing imagery through their global self-attention mechanisms. For example, SETR [32] and Segformer [33] reframe semantic segmentation as a sequence-to-sequence prediction task, pioneering a perspective that shifts from traditional convolutional stacking to global self-attention mechanisms. However, the quadratic complexity of self-attention mechanisms [31] renders them sensitive to training data scale and computational resources, prompting researchers to propose hybrid architectures that balance modeling capability with efficiency. Therefore, some studies, such as UNetFormer [34] and ST-UNet [25], have proposed hybrid architectures combining CNNs and Transformers to balance modeling capacity and computational efficiency. Nevertheless, Zhang et al. [35] point out that both CNN-based and Transformer-based models tend to focus on low-frequency components in images, resulting in insufficient modeling of boundary information and fine-grained semantics.

B. Boundary-Aware Semantic Segmentation

To optimize model prediction accuracy in boundary regions, current research primarily focuses on designing boundary losses, constructing boundary or semantic-aware modules, or indirectly enhancing boundary representation capabilities from the frequency domain perspective. Regarding boundary losses, InverseForm [36] constructs a loss function based on boundary distance that leverages inverse transformation networks to capture spatial transformations between predicted and ground truth boundaries. Wang et al. [37] introduce a boundary loss that predicts differentiable direction vectors to guide predicted boundaries toward progressive alignment with ground truth boundaries. Wang et al. [9] employ a boundary loss function based on geometric similarity that seamlessly integrates boundary guidance into multi-level feature fusion to enhance boundary accuracy. Additionally, other research focuses on constructing boundary or semantic-aware modules to boost boundary feature discrimination. For example, Mask2Anomaly [38] reformulates the segmentation paradigm as mask-level inference. GPINet [22] constructs a geometric prior generation module with iterative updates. BFP [8] and DNLNet [39] explicitly model boundaries as independent semantic entities, while LANet [40] and HSDN [41] propose semantic decoupling strategies to separate features from different categories. These works improve semantic consistency in homogeneous and boundary regions. Furthermore, some studies approach

the problem from a frequency domain perspective. For instance, FsaNet [35] proposes a linear self-attention mechanism targeting low-frequency components, significantly reducing computational overhead while enhancing intra-class consistency and edge contour information. FDNet [42] introduces frequency attention mechanisms to process high and low-frequency information separately, effectively improving image edge preservation and category discrimination capabilities. Meanwhile, PointRend [6] treats image segmentation as a graphics rendering problem and uses an iterative subdivision algorithm to adaptively select points in uncertain boundary regions, enabling point-level segmentation prediction.

However, discriminative learning models inherently tend to prioritize minimizing overall classification errors while neglecting high-frequency boundary information, resulting in insufficient learning and misclassification of boundary pixels [12]. Existing methods essentially improve the inherent limitations of discriminative models without breaking through the framework constraints of discriminative modeling.

C. Diffusion-Based Generative Models

In recent years, diffusion models have garnered widespread attention due to their powerful image generation capabilities. Some research has begun to incorporate diffusion models into segmentation tasks [43],[44],[45]. For example, Baranchuk et al. [46] discovered that intermediate activations in the reverse diffusion process of image generation can effectively capture pixel-level semantic representations for semantic segmentation. [47],[48] explored the implementation of diffusion models in segmentation tasks from a binary segmentation perspective. Additionally, studies such as [49], [50], and [51] have discovered implicitly aligned image-text representations in pretrained diffusion models and explored their applications in semantic segmentation tasks. However, from the perspective of overall segmentation metrics, there remains a significant gap in semantic reasoning accuracy between diffusion generative models and discriminative models [20]. Addressing this issue, DDP [52] replaced the traditional L2 loss in diffusion with cross-entropy loss and constructed a lightweight noise-to-prediction conditional diffusion-aware pipeline. Furthermore, Chen et al. [53] achieved competitive results by introducing bit diffusion models in panoptic segmentation tasks, formulating label generation as a discrete data generation problem.

We observe that discriminative learning excels at capturing low-frequency, large-scale semantic features but struggles to accurately learn high-frequency boundary features. Conversely, diffusion generative learning can effectively capture high-frequency boundary features but lacks accuracy in semantic feature inference. We combine the advantages of both discriminative learning and diffusion generative learning by implementing a conditional guidance network that learns joint guidance representations from coarse segmentation maps predicted by discriminative models and remote sensing images. This effectively guides the diffusion generative model to simultaneously focus on both global semantic structures and boundary details, significantly enhancing both the semantic integrity and boundary accuracy of segmentation results.

III. METHOD

In Section III-A, we first present the methodology for generative semantic segmentation using a latent diffusion model. In Section III-B, we analyze the denoising process of diffusion models from a frequency domain perspective, demonstrating their effectiveness in learning high-frequency components for semantic segmentation. In Section III-C, we introduce our IDGBR framework and detail how it learns joint guidance representations from coarse segmentation maps predicted by discriminative models and remote sensing images through a conditional guidance network, thereby providing effective guidance for the diffusion generative model. Finally, in Section III-D, we present a regularization technique that accelerates the learning process of generative semantic segmentation.

A. Latent Diffusion Model for Generative Semantic Segmentation

In recent years, diffusion models have achieved breakthrough progress in image generation tasks. The core idea of diffusion models is to gradually add noise to data and then learn how to reverse the process through denoising to generate new data samples. Unlike training diffusion models directly in high-dimensional pixel space, latent diffusion models (such as Stable Diffusion [16]) use a pretrained encoder to compress images into smaller latent representations, and subsequently train diffusion models in the latent space, thereby reducing computational complexity. The latent diffusion model typically involves two data modeling processes: the diffusion process and the denoising process. The diffusion process gradually adds Gaussian noise to the latent representation of data, defined as:

$$q(z_t|z_0) = \mathcal{N}(z_t; \sqrt{\bar{\alpha}_t}z_0, (1 - \bar{\alpha}_t)\mathbf{I}) \quad (1)$$

It progressively transforms the sample z_0 into a noisy sample z_t , where $t \in \{0, 1, \dots, T\}$. The constant term $\bar{\alpha}_t := \prod_{s=0}^t \alpha_s = \prod_{s=0}^t (1 - \beta_s)$, where β_s represents the noise schedule [18]. During training, the denoising process typically optimizes a Unet model $\epsilon_\theta(z_t, c, t)$ by minimizing the mean squared error loss, which predicts the noise ϵ added to the noisy sample z_t , under the guidance of condition c :

$$\mathcal{L} = \mathbb{E}_{t, \epsilon} [\|\epsilon - \epsilon_\theta(z_t, c, t)\|_2^2] \quad (2)$$

During inference, random noise z_T is denoised through the denoising model ϵ_θ via a Markov chain under the guidance of condition c , specifically $z_T \rightarrow z_{T-\Delta} \rightarrow \dots \rightarrow z_0$, which can be expressed as:

$$p_\theta(z_{0:T}|c) = p(z_T) \prod_{t=1}^T P_\theta(z_{t-1}|z_t, c) \quad (3)$$

However, latent diffusion models generally assume that sample data is continuous, making them inconvenient for processing discrete label maps. We aim to map discrete label maps to a continuous space while ensuring that the encoded label features can be mapped back to category probability space. Therefore, we additionally learn an embedding network

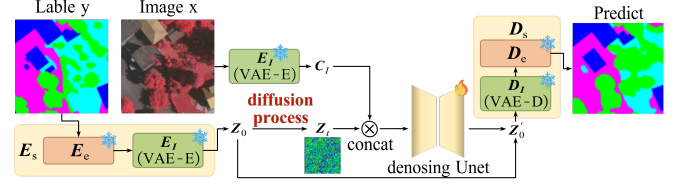


Fig. 2: Generative semantic segmentation pipeline using a latent diffusion model.

consisting of a shallow encoder E_e and a shallow decoder D_e . E_e maps discrete labels to a continuous space, while D_e maps encoded label features back to category probability space. The optimization of the embedding network is independent of the diffusion model and does not require image data. Specifically, E_e contains an embedding layer that maps discrete labels to a 3-channel continuous space, applies a sigmoid function for normalization, and then scales the encoded labels to the range $[-1, 1]$. D_e contains two convolutional layers that first map the 3-channel encoded labels to 128 channels, and then to a K -channel category probability space, where K is the number of categories. To improve the embedding network's robustness during training, we add Gaussian noise (variance = 0.25) to E_e 's output before feeding it to D_e . We optimize the embedding network by minimizing the cross-entropy loss between the category probabilities produced by D_e and the discrete labels.

Given a remote sensing image $x \in \mathbb{R}^{3 \times h \times w}$ and its corresponding segmentation label map $y \in \mathbb{R}^{h \times w}$, the generative semantic segmentation process based on latent diffusion models is illustrated in Fig. 2. Given the image encoder E_I and image decoder D_I from Stable Diffusion, and given the optimized shallow encoder E_e and shallow decoder D_e from the embedding network, we combine E_e with E_I to form encoder E_S for encoding discrete labels, and combine D_e with D_I to form decoder D_S for decoding label features. In our diffusion model training setup, the sample $z_0 = E_S(y)$ and the conditioning information $c_I = E_I(x)$. The diffusion process transforms the sample z_0 into a noisy sample z_t using Equation (1). We concatenate z_t with c_I as input and train the Unet model ϵ_θ to predict the noise added to z_t using Equation (2).

B. Rethinking Diffusion Model from a Frequency Domain Perspective for Semantic Segmentation

In the frequency domain, regions composed of similar neighboring pixels in an image typically manifest as low-frequency components, while edge regions with significant differences between adjacent pixels appear as high-frequency components. Similarly, when segmentation maps are transformed into the frequency domain via Fourier transform, the semantic content generally corresponds to low-frequency components, while boundaries between different semantic regions correspond to high-frequency components. Research has shown that diffusion generative models enhance the learning of high-frequency components in image generation tasks [19], [54]. Therefore, we explore whether diffusion models can

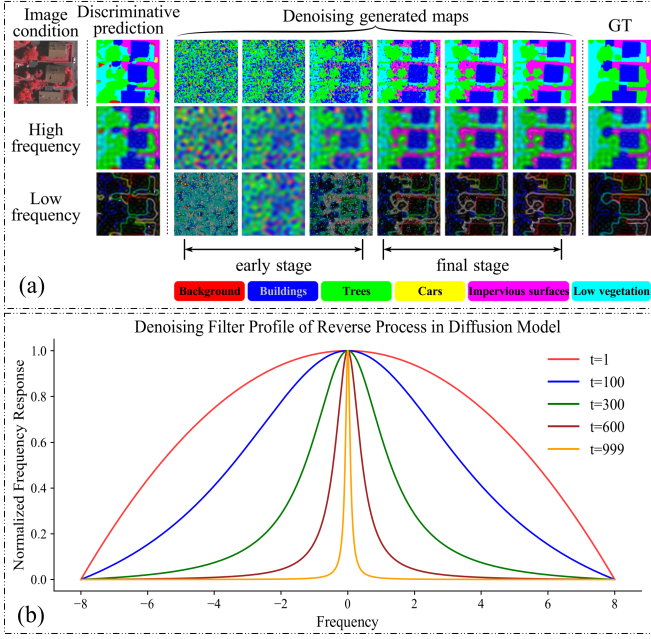


Fig. 3: Analysis of the effectiveness of diffusion-based generative learning for boundary segmentation. (a) Qualitative assessment of inference accuracy on high-frequency and low-frequency components. (b) Theoretical analysis of how the diffusion denoising process enhances high-frequency component learning.

enhance the refinement of object boundaries in semantic segmentation tasks. In this section, we first qualitatively evaluate the accuracy of diffusion-based generative semantic segmentation in inferring both high-frequency and low-frequency components. Subsequently, we theoretically analyze how the diffusion denoising process effectively enhances the model’s ability to learn high-frequency components from input data.

1) Qualitative Evaluation of High/Low-Frequency Components in Diffusion-based Segmentation Maps

We use remote sensing images as conditional information, employing the diffusion process to transform the encoded segmentation label samples z_0 into noisy samples z_t , and train a Unet model to predict the noise added to z_t . During denoising inference, we convert the segmentation maps generated from random noise z_T to the frequency domain via Fourier transform. For clearer observation, we divide the denoising process from z_T to z_0 into two sampling stages: the initial stage from z_T to z_{500} and the final stage from z_{500} to z_0 , where $T = 1000$. Fig. 3 (a) illustrates two interesting phenomena we observed:

The high-frequency components in the generated segmentation maps continuously evolve throughout the entire denoising process, gradually transforming from initially rough and chaotic to refined, and ultimately approaching the geometric contours of the real targets. These high-frequency components reflect positions where semantic changes are most dramatic, such as boundary regions. When noise is introduced into segmentation maps, it typically manifests as random high frequencies that first contaminate the boundary regions, which

are more sensitive to noise. To prevent high-frequency details from being weakened or lost during the generation process, the objective function of diffusion denoising enhances the model’s ability to learn high-frequency components. Compared to segmentation maps predicted by discriminative models, those generated by diffusion models demonstrate significant advantages in boundary region refinement.

The low-frequency components in generated segmentation maps undergo significant changes during the initial stages of denoising but quickly stabilize, showing almost no change in the final stages of denoising. This indicates that the diffusion model’s learning of low-frequency components primarily occurs in the initial sampling interval with high noise. While high-frequency components in segmentation maps represent positions of semantic mutations, the low-frequency components in different regions represent differentiated semantic content in remote sensing images. Therefore, the inference of high-frequency components and low-frequency components in segmentation maps corresponds to two distinct problems: Where do semantic mutations occur? What are the decision boundaries between different semantic categories? Notably, the objective function of generative models does not directly learn decision boundaries between semantic categories, making diffusion generative models less accurate than discriminative models in low-frequency component inference.

2) Why Diffusion Denoising Process Effectively Enhances High-Frequency Component Learning

If we view the diffusion network as a linear filter, the optimal filter derived from the frequency response at each timestep is commonly known as the Wiener filter. Therefore, some studies have used Wiener filters to analyze the denoising process of diffusion models [54], [55]. In this subsection, we further explain the intrinsic reason why diffusion models effectively enhance high-frequency component learning based on the denoising process of the Wiener filtering method. Assuming z_0 is a wide-sense stationary signal, and ε is white noise with variance $\sigma^2 = 1$. For $z_t = \sqrt{\bar{\alpha}_t}z_0 + \sqrt{1 - \bar{\alpha}_t}\varepsilon$, given a linear denoising Wiener filter h_t , the objective function of the diffusion model at time t can be redefined as:

$$\mathcal{J}_t = \|\sqrt{\bar{\alpha}_t}z_0 - h_t * z_t\|^2 \quad (4)$$

Minimizing \mathcal{J}_t in the frequency domain, we obtain the optimal solution of the Wiener filter h_t in the frequency domain, denoted as $\mathcal{H}_t^*(f)$:

$$\mathcal{H}_t^*(f) = \frac{\bar{\alpha}_t |\mathcal{Z}_0(f)|^2}{\bar{\alpha}_t |\mathcal{Z}_0(f)|^2 + (1 - \bar{\alpha}_t) \cdot \sigma^2} \quad (5)$$

where $|\mathcal{Z}_0(f)|^2$ represents the power spectrum of z_0 , and $\mathcal{H}_t(f)$ represents the frequency response of h_t . According to the power-law assumption commonly observed in image power spectra [56], we have $\mathbb{E}[|\mathcal{Z}_0(f)|^2] \approx 1/f^2$. Therefore:

$$\mathcal{H}_t^*(f) \approx \frac{\bar{\alpha}_t}{\bar{\alpha}_t + (1 - \bar{\alpha}_t) \cdot f^2} \quad (6)$$

We plot the normalized $|\mathcal{H}_t^*(f)|$ curves in Fig. 3 (b). Detailed proof is provided in Appendix I.A. The denoising filter initially focuses only on generating low-frequency components

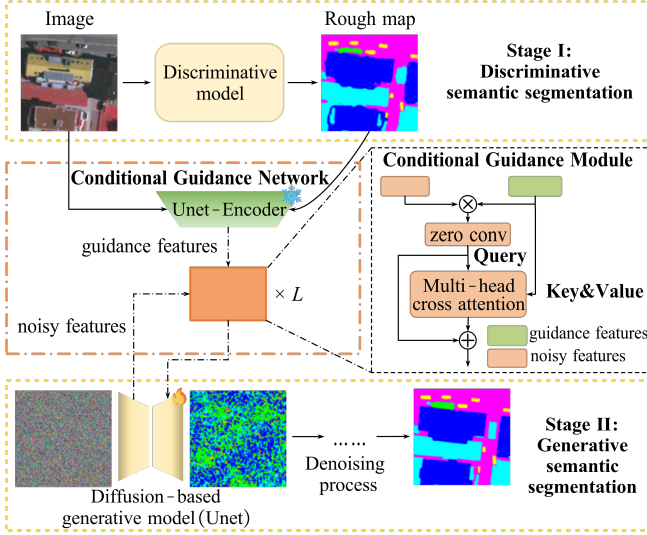


Fig. 4: Unified framework for remote sensing image segmentation merging discriminative models with diffusion generators.

during the early sampling process, and gradually enhances the generation of high-frequency components as t decreases. This indicates that to ensure signal reconstruction, diffusion models pay special attention to and learn high-frequency features in the signal, preventing important edge details from being weakened or lost during generation.

C. The Integration Framework for Boundary Refinement Semantic Segmentation

In the previous subsection, we analyzed diffusion-based generative semantic segmentation from a frequency-domain perspective. Compared to discriminative learning, diffusion generative learning can effectively capture high-frequency boundary features but shows limitations in accurately inferring low-frequency semantic features. To fully leverage the boundary refinement capabilities of diffusion generative models while utilizing the large-scale semantic context from discriminative models, we propose IDGBR, a remote sensing semantic segmentation framework that integrates discriminative and generative models. As illustrated in Fig. 4, the framework consists of a discriminative model, a diffusion generative model, and a conditional guidance network. Training consists of two stages. In the first stage, the discriminative model is trained to obtain coarse segmentation results, serving as conditional guidance for subsequent generative learning. In the second stage, under joint conditional guidance from remote sensing images and coarse segmentation maps, both the conditional guidance network and the diffusion generative model are trained to achieve boundary-refined semantic segmentation.

1) Coarse Discriminative Semantic Segmentation as Conditional Guidance for Generative Learning

Given a remote sensing image $x \in \mathbb{R}^{3 \times h \times w}$ and its corresponding segmentation label map $y \in \mathbb{R}^{h \times w}$, we first train a discriminative model d_θ using cross-entropy loss. This discriminative model can be any conventional semantic

segmentation model. We then use the trained discriminative model to generate coarse segmentation predictions:

$$y_r = d_\theta(x) \quad (7)$$

These coarse segmentation results serve as conditional guidance for generative learning, providing large-scale semantic context information to the generative semantic segmentation training process. In diffusion model training, the sample is defined as $z_0 = E_S(y)$, and the conditional information as $c_I = E_I(x)$ and $c_r = E_S(y_r)$. The functions $E_S(\cdot)$ and $E_I(\cdot)$ denote encoding functions for segmentation maps and remote sensing images, respectively, aimed at transforming input data into low-dimensional latent encoding spaces to reduce computational complexity. The diffusion process transforms sample z_0 into a noisy sample z_t . Under the joint conditional guidance of c_I and c_r , we train a Unet model ϵ_θ to predict the noise added to the noisy sample z_t .

2) Generative Boundary Refinement Semantic Segmentation under Conditional Guidance

(a) Conditional Guidance Network: To better extract joint guiding features from c_I and c_r and to facilitate generative semantic segmentation learning, we design a conditional guidance network. This network consists of a pseudo-siamese Unet encoder and several conditional guidance modules. By employing the pseudo-siamese network structure [57], we can reuse parameters from the pretrained diffusion model's Unet encoder, and utilize long skip connections to pass guidance information to the training diffusion Unet decoder.

We use Stable Diffusion v1.5 [16] as the pretrained diffusion model. The Unet architecture in Stable Diffusion includes 12 encoding modules, 1 middle module, and 12 decoding modules connected via skip connections. The pseudo-siamese encoder in the conditional guidance network comprises 12 encoding modules and 1 middle module from Stable Diffusion's Unet. The outputs from these conditional guidance modules are passed via long skip connections to the 12 decoding modules and 1 middle module in the diffusion Unet. During diffusion Unet training, the pseudo-siamese encoder in the conditional guidance network reuses pretrained parameters and remains frozen; only the conditional guidance module parameters are trained. Fig. 5 illustrates the input and output data flow using one encoding module and its corresponding conditional guidance module in the conditional guidance network as an example.

(b) Conditional Guidance Modules: Each conditional guidance module comprises a zero convolution layer and a cross-attention sub-module. The zero convolution layer merges noisy sample features with conditional guidance features by aggregating local information, capturing local correlations between these features. The cross-attention sub-module further explores global correlations within the fused features across channel dimensions, enhancing global interactions between noisy sample features and conditional guidance features.

Given a pretrained diffusion Unet model, we copy and freeze the encoder parameters from the pretrained Unet to serve as the pseudo-siamese encoder in the semantic guidance network, with parameters denoted as θ_c . The parameters of the

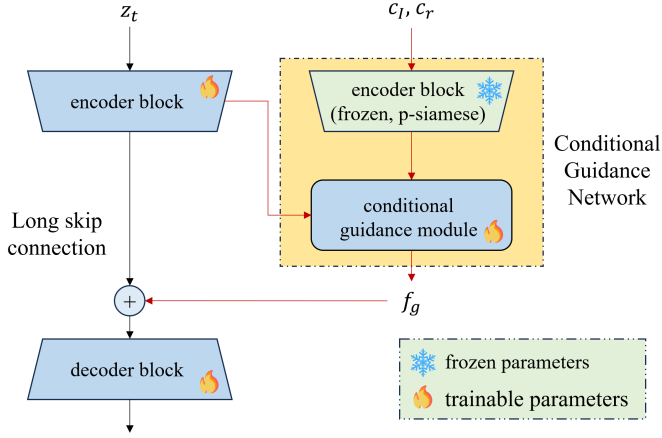


Fig. 5: Input and Output Data Flow of Conditional Guidance Network (Illustrated with an Encoding Module and its Corresponding Conditional Guidance Module)

training diffusion Unet model are denoted as θ . Let $\mathcal{F}(\cdot; \Theta)$ and $\mathcal{F}(\cdot; \Theta_c)$ represent the encoding network modules in the diffusion Unet and pseudo-siamese Unet, respectively. We denote the noisy sample features as $f_{z_t} = \mathcal{F}(z_t; \Theta)$ and the guidance features as $f_c = \text{concat}(\mathcal{F}(c_I; \Theta_c), \mathcal{F}(c_r; \Theta_c))$.

The diffusion Unet and pseudo-siamese Unet are connected through L conditional guidance modules ($L = 13$), as shown in Fig. 4. Each conditional interaction module consists of a 1×1 zero convolution layer and a multi-head cross-attention layer. The zero convolution layer aims to capture local correlations between f_{z_t} and f_c , initialized with zero weights, denoted as $\text{ZConv}(\cdot)$. The output of the zero convolution layer is expressed as:

$$f' = \text{ZConv}(\text{Concat}(f_{z_t}, f_c)) \quad (8)$$

After the convolution operation, we employ cross-attention to further capture global correlations. The multi-head cross-attention layer uses f' as the query Q , and f_c as both key K and value V , realizing:

$$\text{Attention}(Q, K, V) = \text{softmax}\left(\frac{QK^T}{\sqrt{d}}\right) \cdot V \quad (9)$$

where $Q = W_Q \cdot \phi(f')$, $K = W_K \cdot \phi(f_c)$, and $V = W_V \cdot \phi(f_c)$. Here, $W_Q \in \mathbb{R}^{d \times d_e}$, $W_K \in \mathbb{R}^{d \times d_e}$, and $W_V \in \mathbb{R}^{d \times d_e}$ are learnable projection matrices. $\phi(f') \in \mathbb{R}^{N \times d_e}$ and $\phi(f_c) \in \mathbb{R}^{N \times d_e}$ denote the flattening operation applied to f' and f_c , respectively. The enhanced guidance features from the conditional interaction module are represented as:

$$f_g = f' + \text{Attention}(f', f_c, f_c) \quad (10)$$

Both f_g and f_{z_t} are transferred together through long skip connections to the decoder of the diffusion Unet.

3) Regularization Strategy through Representation Alignment for Accelerated Training

Diffusion models have garnered significant attention within deep generative modeling due to their robust generation capabilities and strong performance. However, the high computational cost during both training and inference stages

Algorithm 1 IDGBR Training Process

```

Def train(imgs, labels, rough_labels)
  # imgs: [b, 3, h, w]; labels & rough_labels: [b, 1, h, w]
  # Step 1: Labels Encoding
  labels_embedded = label_embedding(labels)
  rough_embedded = label_embedding(rough_labels)
  # Step 2: VAE Encoding
  img_latents = vae_encode(imgs)
  label_latents = vae_encode(embedded_labels)
  rough_latents = vae_encode(embedded_rough)
  imgs_repr = DINOv2_encode(imgs)
  # Step 3: Diffusion Process
  T = 1000
   $\epsilon$  = random_like(label_latents)
  t = uniform_sample(0, T, size=(B,))
  scaled_t = clamp(T * (1 - (t/T)**3), 0, T-1)
   $\epsilon$ _latents = DDIM(label_latents,  $\epsilon$ , scaled_t)
  # Step 4: Model prediction
  preds_noise, latents_repr = model(noisy_latents,
    img_latents, rough_latents, scaled_t)
   $\mathcal{L}_{\text{REPA}} = -\mathbb{E}[\text{cosine\_similarity}(\text{latent\_repr}, \text{imgs\_repr})]$ 

   $\mathcal{L}_{\text{total}} = \mathcal{L}_{\text{MSE}}(\text{pred\_noise}, \text{noise}) + \lambda \cdot \mathcal{L}_{\text{REPA}}$ 
  return  $\mathcal{L}_{\text{total}}$ 

```

presents a substantial obstacle for their practical application in downstream tasks. In the computer vision domain, existing works optimize and accelerate the training process through various strategies, such as leveraging visual foundation models for representation alignment [20],[58] or enhancing semantic associations via masked modeling [59],[60]. Inspired by the REPA method [20], we utilize DINOv2 [61] as the foundational visual model to facilitate joint representation alignment with the diffusion backbone, thereby accelerating training. The detailed procedure is described in the following two steps:

(a) Visual Representation Extraction: Using pretrained visual encoder f and image x_c , we extract spatial features: $y_c = f(x_c) \in \mathbb{R}^{N \times D}$, where N represents the patch number and D is feature dimensionality.

(b) Diffusion Representation Alignment: At each timestep of the diffusion process, the final-layer hidden state from the Unet encoder is denoted by $h_t = f_\theta(x_t)$. This hidden features is transformed via a learnable MLP module h_ϕ to align with y_c .

$$\mathcal{L}_{\text{REPA}}(\theta, \phi) := -\mathbb{E}_{x_c, \epsilon, t} \left[\frac{1}{N} \sum_{n=1}^N \frac{y_c^{[n]} \cdot h_\phi(h_t^{[n]})}{\|y_c^{[n]}\| \|h_\phi(h_t^{[n]})\|} \right] \quad (11)$$

where n is a patch index and the cosine similarity is computed between corresponding patches.

4) Training & Inference

(a) Training: During the training stage of the diffusion model, the objective is to train the denoising Unet model ϵ_θ to predict the noise ϵ added to the noisy sample z_t , guided by

conditional inputs $c_I = E_I(x)$ and $c_r = E_S(y_r)$. The detailed training algorithm is illustrated in Algorithm 1.

Label encoding: Diffusion models typically assume continuous input data, conflicting with discrete labels in semantic segmentation. Therefore, we design and pretrain a shallow label encoder E_e that maps discrete labels into a continuous differentiable latent space. Specifically, we construct a learnable embedding table for each class, transforming label map $y \in \{0, 1, \dots, K-1\}^{H \times W}$ into a continuous embedding feature $E_0 \in \mathbb{R}^{C \times H \times W}$. This embedding is then normalized to the interval $[-1, 1]$ by:

$$E = 2 \cdot \text{sigmoid}(E_0) - 1 \quad (12)$$

The decoder D_e , composed of two 1×1 convolutional layers, maps the embedded features E back to the label space, producing class probability maps $\hat{y} \in \mathbb{R}^{K \times H \times W}$. During training, we add Gaussian noise to the label embeddings to enhance the label decoder’s ability to recover from embedding perturbations.

Noise schedule strategy: We employ the DDIM scheduler [17], which achieves deterministic sampling through reparameterization of the variance parameters in the diffusion process. We set the noise schedule parameter β_t to increase linearly from 8.5×10^{-4} to 1.2×10^{-2} , covering $T = 1000$ training timesteps. Furthermore, Mou et al. [62] discovered that enhancing conditional guidance during the early stages of the diffusion process significantly improves consistency between images and conditions, as well as the final generation quality. Inspired by this insight, to enhance the semantic perception capability of IDGBR during high-noise stages, we adopt a cubic timestep sampling strategy during training. The cubic timestep sampling formula is defined as follows:

$$t = \left(1 - \left(\frac{t}{T}\right)^3\right) \times T, \quad t \in U(0, T) \quad (13)$$

Joint Training Objective: Under the Stable Diffusion v1.5 framework, we propose a dual-branch joint optimization strategy with a combined loss function consisting of the reconstruction error and representation alignment error. Specifically, this combined loss is defined as a weighted sum of the standard mean squared error loss \mathcal{L}_{MSE} and the representation alignment loss $\mathcal{L}_{\text{REPA}}$:

$$\mathcal{L} = \mathcal{L}_{\text{MSE}} + \lambda \mathcal{L}_{\text{REPA}} \quad (14)$$

Here, \mathcal{L}_{MSE} represents the standard denoising mean squared error loss, while $\mathcal{L}_{\text{REPA}}$ is the representation alignment loss. During the first 500 training steps, we set $\lambda = 0.5$ to incorporate semantic alignment; subsequently, λ is set to 0 to prevent continuous alignment signals from interfering with segmentation learning.

(b) **Inference:** During the inference stage of the diffusion model, we first sample an initial noise $z_T \sim \mathcal{N}(0, \mathbf{I})$ from a standard Gaussian distribution. Then, guided by conditions $c_I = E_I(x)$ and $c_r = E_S(y_r)$, we gradually reverse the diffusion process using the trained denoising network ϵ_θ , recovering the noise-free semantic embedding z_0 through the

Algorithm 2 IDGBR Inferencing Process

```

Def inference(imgs, rough_label):
  # Step 1: Labels Embedding
  embedded_rough = label_embedding(rough_label)
  # Step 2: VAE Encoding
  img_latents = vae_encode(imgs)
  rough_latents = vae_encode(embedded_rough)
  # Step 3: Prepare timesteps
  scheduler.prediction_type =  $\epsilon$ 
  timesteps = scheduler.get_timesteps()
   $\alpha$  = scheduler.alphas_cumprod
  # Step 4: Noise Initialization
  latents = random_like(img_latents)
  # Step 5: Denoising Loop with DDIM update
  for i in range(len(timesteps) - 1):
    t = timesteps[i]
    t_next = timesteps[i + 1]
     $\hat{\epsilon}$  = model(latents, img_latents, rough_latents, t)
     $\bar{\alpha}_t = \alpha[t]$ 
     $\bar{\alpha}_{t'} = \alpha[t_{\text{next}}]$ 
     $\hat{x}_0 = (\text{latents} - \sqrt{1 - \bar{\alpha}_t} * \hat{\epsilon}) / \sqrt{\bar{\alpha}_t}$ 
    latents =  $\sqrt{1 - \bar{\alpha}_{t'}} * \hat{x}_0 + \sqrt{1 - \bar{\alpha}_{t'}} * \hat{\epsilon}$ 
  # Step 6: Decode to Segmentation Map
  decoded = vae_decode(latents)
  seg_logits = label_embedding_decoder(decoded)
  return argmax(softmax(seg_logits), dim=1)

```

DDIM sampler [17]. Finally, we input z_0 into the label decoder to obtain the class prediction map \hat{y} .

IV. EXPERIMENTS

The experiment establishes a comprehensive evaluation system to evaluate the effectiveness and generalizability of the proposed IDGBR semantic segmentation framework across different semantic segmentation tasks and discriminative base models. The evaluation covers representative binary and multi-class remote sensing segmentation tasks, with a focus on assessing IDGBR’s ability to refine high-frequency boundary information from coarse segmentation maps, enhance segmentation quality in complex scenes, and generalize effectively across diverse environments.

A. Datasets

The remote sensing datasets used in this paper can be divided into two types: binary and multi-class segmentation. The binary segmentation datasets include the CHN6-CUG road dataset [63], Fine-Grained Farmland Dataset (FGFD) [64], and WHU Building change detection dataset [65]. The multi-class segmentation datasets include the Potsdam [66] and Vaihingen [67] urban feature classification datasets. Table I provides details about segmentation tasks for each dataset.

The CHN6-CUG road dataset aims to address the representation limitations of existing public datasets in complex road scenes. The dataset was collected from 6 typical urban

TABLE I: Remote sensing semantic segmentation data set used in this paper

Dataset	Segmentation Tasks
CHN6-CUG	Road Segmentation
FGFD	Farmland Segmentation
WHU-Building	Building Segmentation
Potsdam	Landcover Segmentation (six categories)
Vaihingen	Landcover Segmentation (six categories)

areas and annotated by image interpretation experts to cover 12 road subclasses including railways, highways, urban roads, etc. It contains 4,511 images of 1024×1024 pixels at 0.5-meter resolution. In our experiments, all road subclasses were merged into one class, with non-road areas serving as the background class. The dataset was divided into training, validation, and test sets in an 8:1:1 ratio.

The FGFD addresses issues in agricultural remote sensing such as blurred farmland boundaries and severe terrain interference by constructing a refined dataset with sub-meter annotation accuracy. The dataset collects 0.3-meter resolution satellite images from China’s seven major agricultural terrain regions (including 32.9% plateau, 26.1% plain, 8.6% hills, etc.), covering an area of approximately 70 square kilometers. It employs a three-level quality control process of “annotation-cross-validation-expert sampling inspection” to generate 2,606 annotated samples of 512×512 pixels. In our experiments, the dataset was divided into training, validation, and test sets in an 8:1:1 ratio.

The WHU Building change detection dataset is constructed from aerial images with 0.075-meter resolution from two periods: 2012 (post-disaster) and 2016 (post-reconstruction). Geometric registration at 1.6-pixel accuracy was achieved using 30 ground control points. The original data covers 20.5 square kilometers, with annotated buildings increasing from 12,796 to 16,077, capturing the complete evolution of building clusters after the disaster. In our experiments, we cropped the original images to 512×512 pixels and used an 8:1:1 ratio for training, validation, and test sets.

The Potsdam and Vaihingen datasets originate from the ISPRS Test Project on Urban Classification, 3D Building Reconstruction, and Semantic Labeling. Both datasets provide pixel-wise annotations for impervious surfaces, buildings, low vegetation, trees, cars, and background. The Potsdam dataset contains 38 aerial images with a ground sample distance (GSD) of 5 cm. Each image includes a true orthophoto (TOP) and a corresponding normalized digital surface model (nDSM). The orthophotos are available in three formats: infrared-red-green (IRRG), red-green-blue (RGB), and RGB-infrared composite. Each at 6000×6000 resolution. The Vaihingen dataset contains 33 aerial images with a GSD of 9 cm, also including TOP and nDSM data. The TOP images in this dataset are provided in a near-infrared-red-green (NIR-RG) format with a resolution of 2494×2064 resolution. All images are cropped to 512×512 patches, yielding 3456 training and 2016 test images for Potsdam, and 562 training and 180 test images for Vaihingen.

B. Experiment Settings

1) Implementation Details

To assess IDGBR’s generalization in improving boundary quality of coarse segmentation maps generated by different base models, we conducted further experiments across multiple base segmentation models spanning four architectural paradigms: (1) CNN architectures: DeepLabv3+ [68] and LSKNet [29]; (2) Transformer-based architecture: SegFormer [69]; (3) Self-supervised learning: Using frozen DINOv2 [61] pretrained weights as visual encoder with Mask2Former’s fine-tunable segmentation head; (4) Generative model architecture: DDP [52] with end-to-end predictions. Coarse labels from the first three paradigms served as conditional inputs for IDGBR boundary optimization, while DDP predictions served only as a baseline for comparing segmentation results.

For the base discriminative training, all base discriminative segmentation models used default hyperparameters and were implemented using open-source libraries. We employed standard data augmentation strategies: (1) random resizing with aspect ratio preserved between 0.5 and 2.0 (output size 512×512); (2) random cropping at size 512 ensuring no class exceeds 75% coverage; (3) horizontal flipping with 50% probability; (4) random adjustments to brightness, contrast, and saturation. All models were trained with a batch size of 8 for 20k iterations.

During the training of IDGBR, we employ a Unet network initialized with the pretrained weights of Stable Diffusion v1.5 as the backbone for the denoising process. Both images and labels are separately encoded using VAE encoders, and the resulting representations are concatenated to serve as conditional inputs. To avoid biases arising from model configuration, the training and inference procedures of IDGBR are kept consistent across different tasks and backbone models; for different numbers of classes, only the output projection dimension is modified during inference. Specifically, IDGBR model is trained for 80,000 iterations with a batch size of 4 and a fixed learning rate of $1e-5$. Inference is performed over 25 steps, with a classifier-free guidance weight of 3. To accelerate model convergence, a representation alignment mechanism is introduced during early training. Concretely, feature maps from the final layer of the Unet downsampling stage are first extracted and projected to semantic dimensions using a three-layer linear projection module, while a single linear expansion module handles spatial dimensional matching. The transformed features are then aligned with the semantic representations extracted by DINOv2, using cosine similarity as the alignment objective. This mechanism is only activated during the first 200 training steps to guide the model toward more efficient semantic learning.

2) Evaluation Metrics

In remote sensing semantic segmentation, the accuracy and integrity of boundaries are among the key factors ensuring the practical utility of mapping results. Margolin et al. [70] pointed out that current mainstream evaluation metrics (such as IoU, mean F1, AP, and AUC) suffer from issues including ignoring the spatial dependencies between pixels and overlooking the varying importance of different prediction errors. Due to

significant intra-class variability, blurred inter-class boundaries, challenges in foreground-background separation, and complex scenes inherent in remote sensing imagery, semantic segmentation tasks frequently exhibit insufficient boundary granularity and scattered patch fragments within segmented regions. These issues are prevalent and severely constrain the reliability of downstream tasks like object extraction and land cover statistics. This bottleneck stems from the lack of precise quantification of boundary structures in mainstream metrics, making it difficult to accurately capture model improvements in addressing boundary discontinuities, displacement, blurry transitions, or spurious patch corrections.

To overcome the limitations of the aforementioned evaluation assumptions, we incorporate the boundary-sensitive evaluation metric WF-measure [70] (hereafter referred to as WFm). This metric extends the conventional F_β measure to continuous domains and introduces a spatially sensitive weighting mechanism, enabling it to effectively assess the geometric fidelity of segmentation results. The calculation formula for WFm is as follows:

$$F_\beta^w = \frac{(1 + \beta^2) \cdot \text{Precision}_w \cdot \text{Recall}_w}{\beta^2 \cdot \text{Precision}_w + \text{Recall}_w} \quad (15)$$

$$\text{Precision}_w = \frac{TP_w}{TP_w + FP_w} \quad (16)$$

$$\text{Recall}_w = \frac{TP_w}{TP_w + FN_w} \quad (17)$$

Among these, Precision_w and Recall_w represent weighted precision and weighted recall, respectively. The four weighted terms TN_w , TP_w , FP_w , and FN_w are derived from traditional definitions via continuous value extension and incorporating of spatial dependency relationships and position-sensitive weight calculations. In our experiments, the boundary tolerance of WFm is set to 3 pixels (denoted as 3px) and the β value is set to 1, providing a unified measure for evaluating the boundary quality of different models.

C. Evaluation on Binary Segmentation Tasks

In binary Segmentation, we construct a validation framework using three representative binary remote sensing tasks: road segmentation, building extraction, and cropland delineation. These three tasks correspond to testing ground object features with linear extension, geometric regularity, and texture complexity, respectively, effectively evaluate IDGBR's boundary reconstruction capability and target perception capabilities for objects with different morphological characteristics across various discriminative baseline models.

1) Evaluation on Road Segmentation

The complex topological structures and multi-scale characteristics of roads in the CHN6-CUG dataset provide an effective evaluation benchmark for evaluating the model's capability in boundary refinement and connectivity restoration capabilities for linear features. Comparative results are presented as follows:

TABLE II: Quantitative results (%) of different methods on the CHN6-CUG road dataset.

Method	DiscModel Backbone	Road		Kappa	OA	WFm (3px B)
		IoU	F1score			
DDP	ConvNext-t	64.19	78.19	77.76	97.59	36.52
DeepLabV3+	ResNet-50	62.59	76.99	75.66	97.48	34.44
DeepLabV3+→ours	ResNet-50	62.94	77.25	75.84	97.34	36.49
SegFormer	MIT-B5	64.13	78.14	76.82	97.50	36.00
SegFormer→ours	MIT-B5	64.54	78.45	77.12	97.50	37.64
DINOv2	ViT-B/14	57.37	72.91	71.30	96.96	27.93
DINOv2→ours	ViT-B/14	61.07	75.83	74.33	97.17	34.65
LSK	LSK-s	62.46	76.89	75.54	97.44	35.90
LSK→ours	LSK-s	63.30	77.53	76.19	97.47	37.31

As shown in Table II, analysis based on the WFm boundary metric demonstrates that optimizing boundaries with the proposed IDGBR framework leads to significant improvements in boundary scores for models such as DeepLabV3+, SegFormer, DINOv2, and LSK, indicating strong cross-model generalization capability. In terms of the IoU metric, all baseline models achieved consistent improvements after boundary optimization, with DINOv2 achieving the most notable gains. In addition, although the DDP model, as a diffusion-based benchmark, achieves overall accuracy comparable to discriminative methods after adaptation to downstream tasks, its WFm remains lower than that of models optimized by IDGBR.

Discriminative models commonly exhibit three typical deficiencies when dealing with complex road scenarios: (1) Insufficient precision in high-frequency edge segmentation, (2) Incomplete delineation of topological structures in complex road networks, and (3) Inadequate preservation of road network structural continuity. As shown in Fig. 6, we perform a comparative analysis of different segmentation models across three representative scenarios. In narrow road scenarios shown in Fig. 6 (a), baseline discriminative models often suffer from significant omission errors, demonstrating their substantially limited ability to perceive low-contrast elongated structures. In contrast, our optimized model can effectively enhance the perception of such low-visibility features based on coarse segmentation results, achieving significant improvements in segmentation completeness. Fig. 6 (b) illustrates a complex highway scene with intersections and overpasses. Discriminative models struggle to maintain road integrity and connectivity when handling overlapping structures and complex topological structures, leading to incomplete geometric features of the extracted roads. Our approach refines road edge details and supplements topological relationships based on the initial coarse predictions. Fig. 6 (c) illustrates road scenarios under high-contrast illumination conditions. Under strong illumination gradients, drastic high-frequency variations tend to mislead discriminative models into overfitting to artifact features at light-shadow boundaries, resulting in structural omissions and topological misinterpretations in shaded areas. Through iterative boundary optimization, our method significantly improves the edge localization precision of baseline models in unevenly illuminated regions with complex shadows.

2) Evaluation on Cultivated Land Segmentation

As shown in Table III, IDGBR achieved an average WFm improvement exceeding 9.08%, significantly improving the

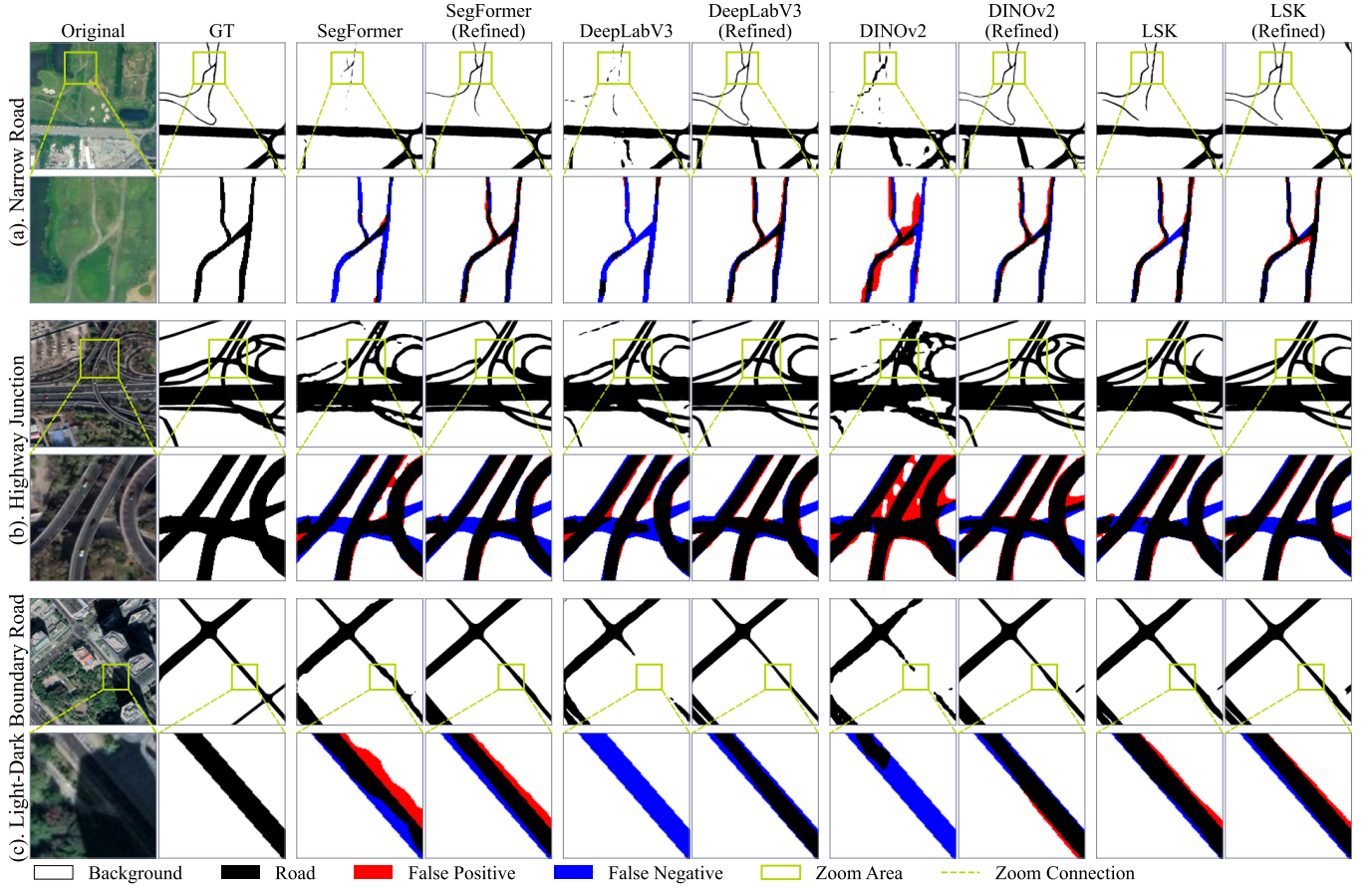


Fig. 6: Qualitative analysis on the CHN6-CUG road dataset, including DeepLabV3+, SegFormer, and DINOv2 methods and their results enhanced by IDGBR. Blue indicates false negatives (segmentation omissions), and red indicates false positives (segmentation commissions).

TABLE III: Quantitative results (%) of different methods on FGFd.

Method	DiscModel Backbone	Farmland		Kappa	OA	WfM (3px B)
		IoU	F1score			
DDP	ConvNext-t	87.44	93.30	83.86	92.16	42.40
DeepLabV3+	ResNet-50	86.15	92.56	82.56	91.47	39.66
DeepLabV3+→ours	ResNet-50	86.36	92.68	82.83	91.60	49.35
SegFormer	MIT-B5	87.51	93.34	84.13	92.27	41.84
SegFormer→ours	MIT-B5	87.66	93.42	84.36	92.39	49.78
DINOv2	ViT-B/14	84.77	91.76	80.73	90.57	33.60
DINOv2→ours	ViT-B/14	85.85	92.39	82.16	91.27	46.73
LSK	LSK-s	87.61	93.39	84.22	92.32	43.82
LSK→ours	LSK-s	87.77	93.49	84.48	92.44	49.38

usability of extracted field parcels. The IDGBR-refined segmentation results of DINOv2 showed the greatest enhancement, with WfM rising 13.13% to 49.78%. For other models, IDGBR boosted WfM by 9.69% on DeepLabV3+, 7.94% on SegFormer, and 5.56% on LSK, further demonstrating its effectiveness.

3) Evaluation on Cross-Phase Building Segmentation

In the initial post-disaster phase (Table IV), IDGBR brought significant improvements across all baseline models in every evaluation metric. For DeepLabV3+, SegFormer, and DINOv2, the WfM increased by 6.55%, 4.75%, and 8.95%,

TABLE IV: Quantitative results (%) in the post-disaster phase of the WHU Building dataset.

Method	DiscModel Backbone	Building		Kappa	OA	WfM (3px B)
		IoU	F1score			
DDP	ConvNext-t	93.03	96.39	95.75	98.91	69.44
DeepLabV3+	ResNet-50	93.00	96.37	95.73	98.91	68.41
DeepLabV3+→ours	ResNet-50	94.37	97.11	96.59	99.13	74.96
SegFormer	MIT-B5	93.58	96.68	96.10	99.00	71.16
SegFormer→ours	MIT-B5	94.72	97.29	96.81	99.18	75.91
DINOv2	ViT-B/14	91.32	95.46	94.66	98.64	62.64
DINOv2→ours	ViT-B/14	93.45	96.61	96.02	98.98	71.59
LSK	LSK-s	95.02	97.45	96.99	99.23	78.14
LSK→ours	LSK-s	95.23	97.56	97.12	99.26	78.73

TABLE V: Quantitative results (%) in the post-reconstruction phase of the WHU Building dataset.

Method	DiscModel Backbone	Building		Kappa	OA	WfM (3px B)
		IoU	F1score			
DDP	ConvNext-t	92.97	96.35	95.52	98.64	72.23
DeepLabV3+	ResNet-50	91.70	95.67	94.69	98.40	66.59
DeepLabV3+→ours	ResNet-50	92.73	96.23	95.37	98.60	71.87
SegFormer	MIT-B5	92.49	96.10	95.22	98.57	71.64
SegFormer→ours	MIT-B5	93.06	96.41	95.59	98.67	73.95
DINOv2	ViT-B/14	90.78	95.17	94.07	98.22	61.78
DINOv2→ours	ViT-B/14	92.84	96.29	95.44	98.62	70.63
LSK	LSK-s	91.81	95.73	94.77	98.43	70.81
LSK→ours	LSK-s	91.93	95.79	94.84	98.45	71.18

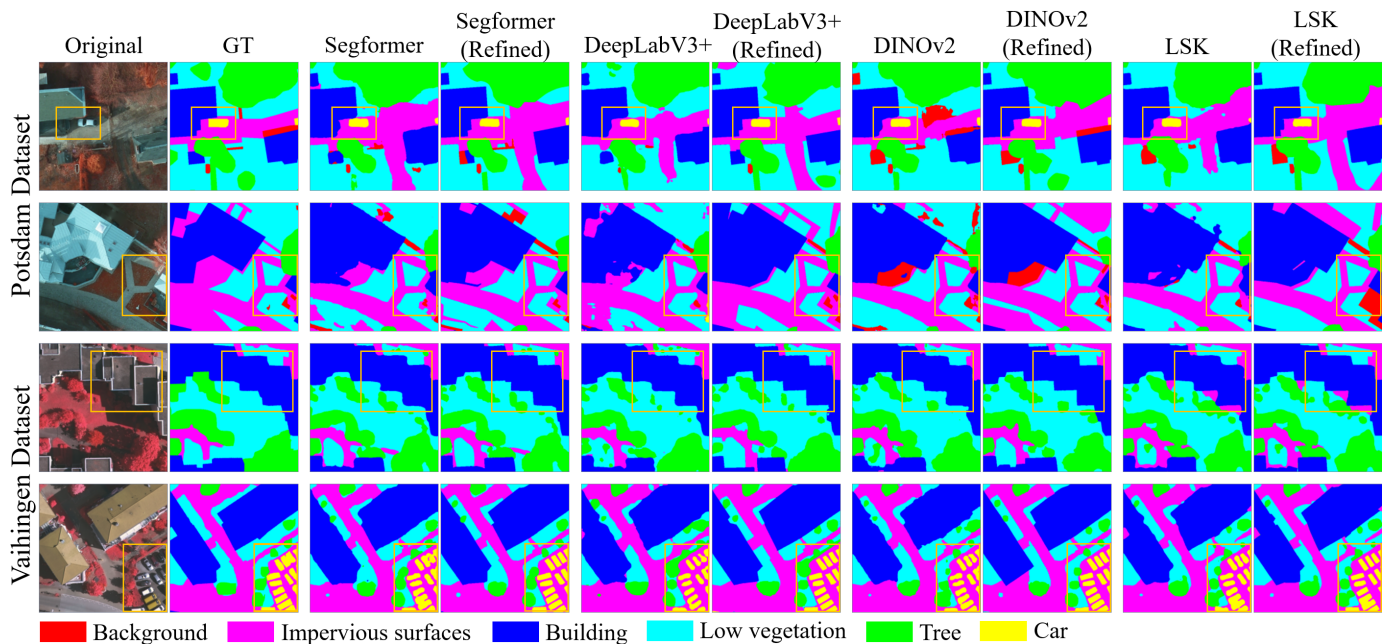


Fig. 7: Qualitative results of different methods on multi-class segmentation dataset.

TABLE VI: Quantitative results (%) of different methods on the Potsdam dataset.

Method	DiscModel-Backbone	Impervious surfaces	Building	Low vegetation	Tree	Car	mean F1	mIoU	WFm (3px B)
DDP	ConvNext-t	93.13	96.67	86.56	86.24	91.3	90.78	83.36	41.11
DeepLabV3+	ResNet-50	93.18	96.95	86.51	86.07	91.63	90.87	83.53	37.40
DeepLabV3+→ours	ResNet-50	93.21	96.91	86.15	85.45	92.07	90.76	83.37	42.14
SegFormer	ViT-B/14	92.87	96.16	86.82	86.06	91.42	90.67	83.15	39.71
SegFormer→ours	ViT-B/14	93.06	96.34	86.77	85.70	92.04	90.78	83.36	42.59
DINOv2	MIT-B5	92.53	96.55	85.98	86.11	90.88	90.41	82.74	35.12
DINOv2→ours	MIT-B5	92.86	96.61	86.16	85.33	92.10	90.61	83.12	43.24
LSK	LSK-s	92.10	95.89	85.67	84.91	91.82	90.08	82.22	38.28
LSK→ours	LSK-s	92.70	96.27	85.92	84.94	91.84	90.33	82.65	42.76

respectively. IDGBR maintained stable performance in cross-phase testing (Table V). Taking DeepLabV3+ as an example, its WFm improved from 68.41% to 74.96% (+6.55%) and IoU rose from 93.00% to 94.37% in the post-disaster phase; while maintaining 71.87% WFm (+5.28%) and achieving 92.73% IoU (from 91.70% baseline) in the post-reconstruction phase. At the macro level, IDGBR yielded average improvements of 5.21% in WFm and 1.21% in IoU during the post-disaster phase, while achieving gains of 4.20% (WFm) and 0.95% (IoU) in the post-reconstruction phase, which demonstrates IDGBR’s robust cross-temporal adaptability.

D. Evaluation on Multi-Class Segmentation Tasks

In multi-class segmentation, we employ Potsdam and Vaihingen as benchmark datasets, conducting comparative analyses of model performance in complex boundary scenarios (such as building edges, fragmented vegetation boundaries, vehicle contours, etc.). This approach validates the effectiveness of our method in optimizing boundary regions within multi-class segmentation tasks.

1) Evaluation on Potsdam Dataset

From the experimental results in Table VI, IDGBR framework achieves superior boundary refinement by synergistically integrating the semantic discriminability of discriminative models with the edge delineation strengths of diffusion models, outperforming both conventional discriminative baselines and DDP in segmentation precision. Notably, IDGBR achieved substantial improvements in WFm metrics across all tested models, with gains ranging from 2.88% to 8.12%, where DINOv2 demonstrated the most remarkable enhancement from 35.12% to 43.24%. Meanwhile, the method maintained stable mIoU performance across different architectures, demonstrating that IDGBR successfully enhances boundary precision without compromising overall segmentation quality.

2) Evaluation on Vaihingen Dataset

The experimental results on the Vaihingen dataset, as shown in Table VII, demonstrate that compared to discriminative baseline models, our framework effectively improves both WFm and mIoU across different model architectures. Regarding the WFm metric, our framework yielded improvements of 4.76%, 1.28%, 1.28%, and 2.40% for DeepLabV3+, SegFormer, DINOv2, and LSK, respectively, further validating our method’s enhancement of boundary representation capabilities.

TABLE VII: Quantitative results (%) of different methods on the Vaihingen dataset

Method	DiscModel-Backbone	Impervious surfaces	Building	Low vegetation	Tree	Car	mean F1	mIoU	WFm (3px B)
DDP	ConvNext-t	89.50	94.53	81.68	88.23	81.93	87.17	77.60	45.68
DeepLabV3+	ResNet-50	88.92	94.04	80.27	87.45	78.98	85.93	75.76	40.38
DeepLabV3+→ours	ResNet-50	89.37	94.52	80.58	87.65	81.83	86.79	77.03	45.14
SegFormer	MIT-B5	90.04	95.10	81.64	87.96	82.15	87.38	77.95	43.76
SegFormer→ours	MIT-B5	90.11	95.26	81.75	87.97	82.53	87.52	78.17	45.04
DINOv2	ViT-B/14	88.38	94.14	80.98	87.10	76.64	85.45	75.09	37.88
DINOv2→ours	ViT-B/14	88.55	94.29	81.00	87.14	77.89	85.77	75.54	39.16
LSK	LSK-s	89.35	94.65	81.10	87.63	82.46	87.04	77.39	42.62
LSK→ours	LSK-s	89.47	95.13	81.34	87.88	82.69	87.30	77.82	45.02

in multi-class remote sensing segmentation tasks.

In both Potsdam and Vaihingen datasets, as evidenced in Fig. 7, the optimized segmentation results consistently restore spatial structures of discretely distributed small patches and irregular segments (such as vehicle boundaries and vegetation fragments). Additionally, for objects with strong geometric structures (such as buildings and road edges), the consistency between spatial topological relationships and actual ground object distribution is significantly improved after optimization.

V. DISCUSSION

A. Enhancing Semantic Awareness in Diffusion Inference: Effects of Conditional Guidance and Cubic Timestep Sampling

This section mainly discusses the applicability and limitations of diffusion models in semantic segmentation, with analysis conducted at two levels: (1). Exploring the role of conditional guidance in category discrimination and boundary refinement in diffusion models; (2). Exploring the role of cubic timestep sampling mechanism to improve overall performance and semantic consistency. Specifically, the experiments use SegFormer as the discriminative baseline model and are conducted on both the Potsdam and Vaihingen datasets.

In the proposed IDGBR framework, we use remote sensing images and rough labels as conditional guidance, and introduce a cubic timestep sampling strategy to enhance semantic representation capabilities. To systematically assess the contribution of each component, we designed three ablation experiments, which can be divided into three groups: (1). Experiment A: using only remote sensing images as guidance; (2). Experiment B: using remote sensing images and rough labels jointly guided by the proposed Conditional Guidance Module; (3). Experiment C: introducing cubic timestep sampling technique into the timestep sampling based on Experiment B. As shown in Table VIII, we compared three different strategies: “Image” refers to the use of remote sensing image guidance, “Rough” refers to the use of rough label guidance, and “Cubic” refers to the additional use of the cubic timestep sampling technique; check marks and crosses are used to indicate whether the corresponding feature is enabled.

By comparing the three sets of experimental results, Experiment A recorded the lowest WFm values (33.66% on CHN6-CUG; 30.39% on Potsdam) along with significantly reduced mF1 and mIoU versus other groups. This indicates that without rough label guidance, the model struggles to

capture object boundaries. In Experiment B, WFm of the two datasets increased to 37.64% and 40.34% respectively, and the mIoU also improved substantially. This demonstrates that rough labels as additional semantic guidance play a crucial role in boundary modeling. In Experiment C, WFm in the Potsdam dataset further increased to 42.59%, with other metrics also showing an upward trend. This indicates that cubic timestep sampling strengthens feature discrimination at semantic boundaries across multiple classes. However, in the binary segmentation CHN6-CUG dataset, this strategy led to a slight decrease in all metrics. This phenomenon can be attributed to differences in task requirements. Binary segmentation requires precisely capture significant feature differences between local specific targets and their backgrounds, without considering complex feature relationships among other irrelevant targets in the global scene. The cubic sampling strategy, by increasing sampling frequency in high-noise regions, forces the diffusion model to allocate more attention to subtle feature differences among various potential targets throughout the entire scene, significantly enhancing the model’s discriminative ability in multi-class segmentation tasks. However, this shift in feature learning direction interferes with binary segmentation task learning, causing the model to no longer focus on learning the most significant discriminative features between a single target and its background, thereby weakening the model’s precision in single-target discrimination. Experiments validate that integrating the Conditional Guidance Module with cubic timestep sampling in IDGBR significantly boosts boundary quality and the processing of complex semantic structures in multi-class segmentation tasks.

B. Discussion on Applicability and Limitations

We categorize errors in rough labels into two types: semantic boundary errors and semantic content errors. For semantic boundary errors in rough labels, experimental results demonstrate the outstanding capability of our proposed method to optimize semantic boundaries in both binary and multi-class classification tasks. For semantic content errors in rough labels, our method exhibits dependence on the completeness of information in correct patches.

Based on the completeness of information in correct patches, this dependency can be divided into three progressive levels:

TABLE VIII: Qualitative results (%) of our framework under different guidance conditions on CHN6-CUG and Potsdam datasets.

Setting	Requirements			CHN6-CUG			Potsdam		
	Image	Rough	Cubic	mean F1	mIoU	WFm (3px B)	mean F1	mIoU	WFm (3px B)
Experiment A	✓	✗	✗	85.34	76.66	33.66	73.89	58.90	30.39
Experiment B	✓	✓	✗	88.56	80.96	37.64	89.29	80.88	40.34
Experiment C	✓	✓	✓	87.96	80.14	37.16	90.78	83.36	42.59

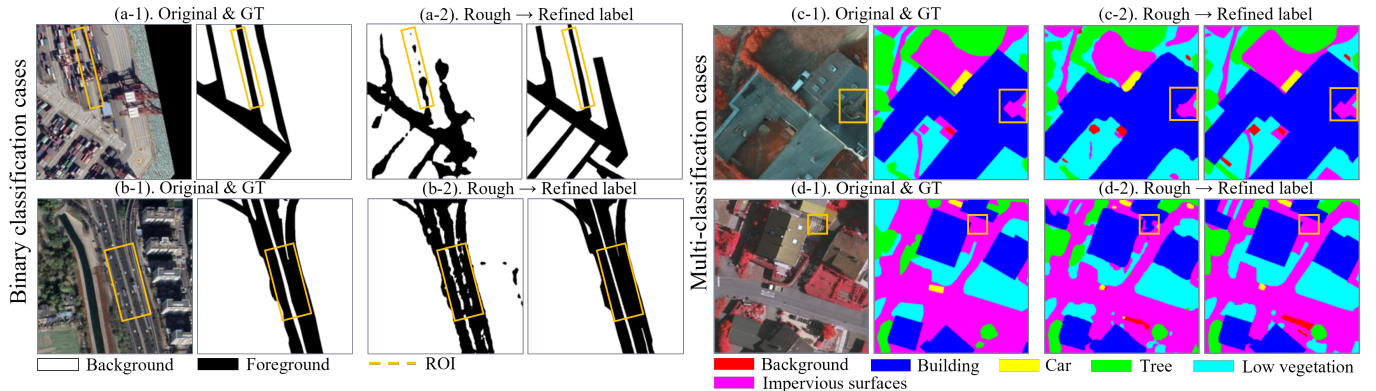


Fig. 8: Examples of complete semantic patch restoration.

When semantic patches exhibit partial segmentation omissions or commissions, yet the correct patch regions can still approximately represent or deduce complete information through semantic adjacency relationships, our method effectively repairs erroneous semantics. Fig. 8 showcases complete semantic patch restoration cases. (i) In (a-2), the rough label shows massive segmentation omissions on the left side of the road (ROI), but the scattered correct patches are sufficient to reveal the length and width of the road area. The spatial distribution patterns of roads have already been learned by the generative model during its training on the road annotation dataset. During inference, these scattered patches are sufficient to activate the road geometric structure prior in the model weights, thereby completing the global supplementation of the semantic patch. (ii) In (b-2), the spatial position of the road patch is basically correct, but its internal structure appears fragmentation. The road continuity patterns learned by the model during training effectively correct the local errors within the patch. (iii) In (c-2), the spatial positions of impervious surface and low vegetation patches within the ROI region are generally correct, yet boundary delineations between patches show imprecision. The model addresses these edge-related semantic inaccuracies through boundary refinement mechanisms. (iv) In (d-2), the impervious surface patch in the ROI region was misclassified as building categories, but the model corrected these scattered classification errors by utilizing the continuity patterns of impervious surfaces.

When semantic patches exhibit partial segmentation omissions or commissions, yet correct patch regions can only infer localized information through semantic adjacency relations, our method only correct the relevant local semantics. Fig. 9 showcases partial semantic patch restoration. (i) In (a-2), the

majority of the non-cultivated land within the ROI were misclassified. Although scattered background patches activated the farmland boundary continuity patterns learned by the model from the farmland dataset, this was insufficient to support complete reconstruction of the patch width. Consequently, the optimization could only refine the slender structure of the non-cultivated land. (ii) In (b-2), there are only a few road semantic patches at the bottom of the ROI. The road geometric patterns learned by the model during training can geometrically correct this area but are insufficient to infer the length information of the road. (iii) In (c-2), building patches in the ROI were misclassified as background. The building area in the image was under construction, with texture features significantly different from surrounding buildings, making it difficult for the model to identify incorrect patches by comparing the image with rough labels. (iv) In (d-2), low-rise buildings on the left side of the ROI region were misclassified as impervious surfaces due to radiometric distortion caused by shadow interference from adjacent high-rise structures on the right. The model could correct the misclassified patches on the right through image and coarse label comparison, but the shadow-affected areas on the left side remained uncorrected.

When semantic patches exhibit complete omissions or commission errors, and the semantic content cannot be reliably inferred from adjacent patches, our method is unable to rectify these inaccuracies. Fig. 10 showcases instances where incorrect semantic patches cannot be restored. (i) In (a-2), correctly classified semantic patches within the ROI are fragmented and lack farmland characteristics and spatial continuity, resulting in their removal as noise by the model. (ii) In (b-2), the gap between the left and right buildings in the ROI with ambiguous boundaries, leading the model to misidentify them as a single

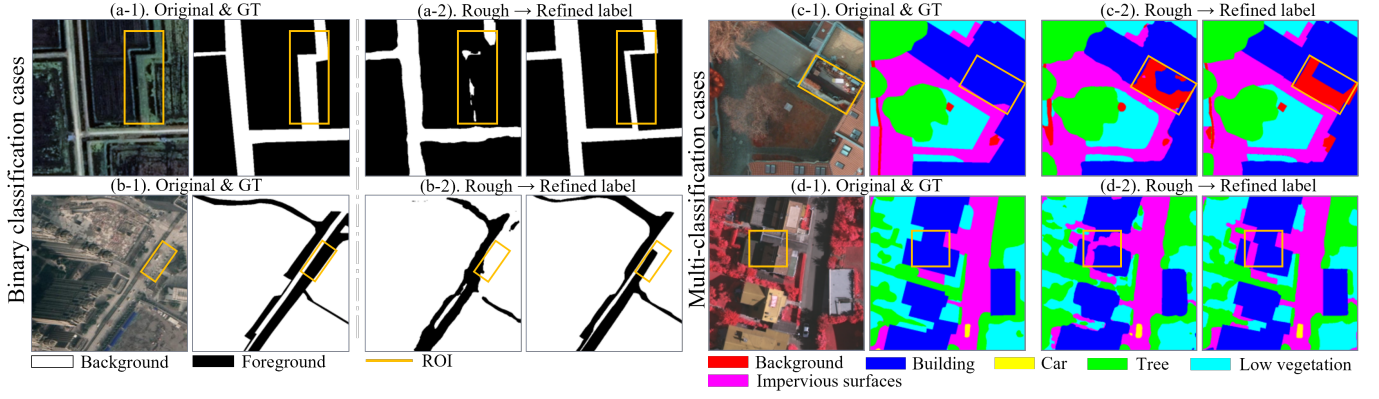


Fig. 9: Examples of partial semantic patch restoration.

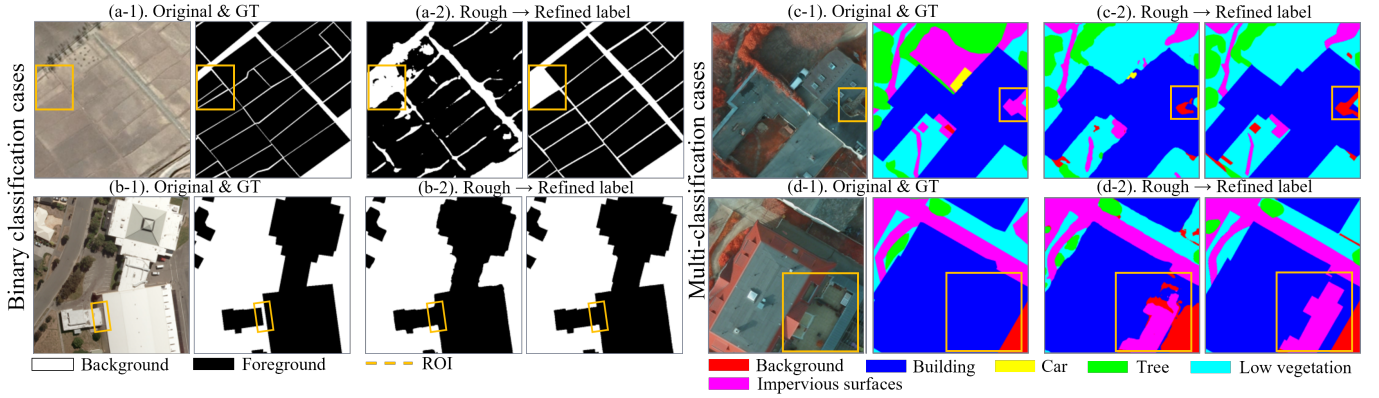


Fig. 10: Examples of irreparable incorrect semantic patches.

connected region despite comparing the image with rough labels. (iii) In (c-2), impervious surface patches in the ROI were misclassified as background. Despite comparing the image with coarse labels, the model corrected only the geometric errors while failing to address the semantic misclassification. (iv) In (d-2), building patches in the ROI were misclassified as impervious surfaces. The area shows open-air renovated balconies that closely resemble impervious surfaces in texture and color, causing the model to fail to detect the semantic errors in the rough labels.

C. Speeding Up Representation Learning through Incipient Alignment Strategies

Fig. 11 The impact of representation alignment mechanism and alignment strength (λ) on model performance using CHN6-CUG and Potsdam datasets, divided into four experimental groups. The *w/o Align* ($\lambda = 0$) group represents training without representation alignment; the break control group stops alignment at step 200.

As shown in Fig. 11, mIoU comparisons between non-aligned (*w/o Align*) and aligned ($\lambda = 0.25, 0.5$) conditions demonstrate the efficacy of representation alignment. It is evident that introducing the representation alignment strategy significantly accelerates the model’s performance improvement rate in the early stages of training on both datasets.

On the CHN6-CUG dataset, introducing the representation alignment strategy significantly accelerated the model’s performance improvement within the first 200 steps. In contrast, after 1000 steps, the mIoU metric of the non-aligned group gradually surpassed that of the aligned group, indicating that overly strong alignment may inhibit the model’s autonomous ability to model task-specific semantics.

On the Potsdam dataset, representation alignment with $\lambda = 0.5$ demonstrated optimal performance across all training stages. In the experiment with $\lambda = 0.5$, after stopping the representation alignment, the model showed notably higher convergence efficiency compared to the group without alignment.

In both tasks, all experiments using representation alignment showed a trend of diminishing performance gains or even decline after 400 steps, whereas models without alignment remained more stable. Therefore, we only applied representation alignment in the early training stages to avoid interference with the model’s learning of task-specific semantics during later stages.

D. Effects of Boundary Tolerance Thresholds in WF-measure

To assess boundary threshold sensitivity in WF-measure, we evaluated three tolerance margins: 1px, 3px, and 5px. The boundary metric WFm was calculated using the SegFormer

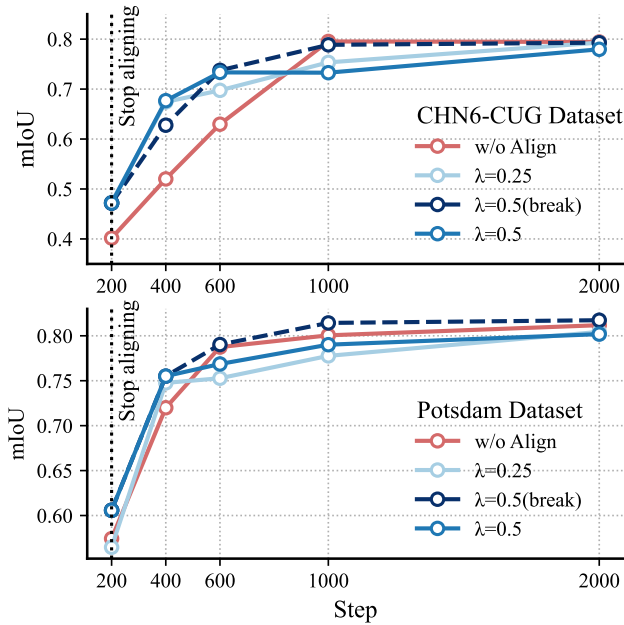


Fig. 11: The impact of representation alignment mechanism and alignment strength (λ) on model performance using CHN6-CUG and Potsdam datasets. The w/o Align ($\lambda = 0$) group represents training without representation alignment; the break control group stops alignment at step 200.

model on both the Potsdam and Vaihingen datasets, with results shown below:

TABLE IX: Boundary accuracy results (%) of our framework under different boundary thresholds on the Potsdam and Vaihingen datasets

Boundary	Method	WfM	
		Potsdam	Vaihingen
1px	SegFormer	26.92	28.46
	SegFormer \rightarrow IDGBR	29.75 (+2.83)	29.65 (+1.19)
3px	SegFormer	39.71	43.76
	SegFormer \rightarrow IDGBR	42.59 (+2.88)	45.04 (+1.28)
5px	SegFormer	47.42	53.24
	SegFormer \rightarrow IDGBR	49.90 (+2.48)	54.36 (+1.12)

The results (shown in Table IX) demonstrate that as the threshold increases, the WfM exhibits an overall upward trend, which aligns with the expectation that higher tolerance relaxes boundary matching requirements. Meanwhile, IDGBR maintains steady WfM metric gains across all thresholds, with relatively small variations in improvement magnitude at different threshold levels (2.48%–2.88% for Potsdam and 1.12%–1.28% for Vaihingen). This indicates that the IDGBR framework is insensitive to boundary tolerance changes and demonstrates robust accuracy consistency.

VI. CONCLUSION

In this work, we address the issue of inaccurate boundary delineation in remote sensing semantic segmentation. First, we observe that discriminative learning excels at capturing low-frequency features but exhibits inherent limitations in learning high-frequency features for semantic segmentation.

Subsequently, we validate through qualitative experimental analysis and quantitative theoretical proof that the diffusion denoising process significantly enhances the model’s capability to learn high-frequency features. We further observe that these models lack sufficient semantic inference capabilities for low-frequency features when solely guided by the original image. Consequently, we integrate the strengths of discriminative learning and diffusion-based generative learning to propose IDGBR. This framework employs a conditional guidance network to learn joint guidance representation from the coarse segmentation map and the input image, thereby leveraging the respective advantages of discriminative and generative models in semantic and boundary aspects. We conducted extensive experiments on CNN-based architectures, Transformer-based architectures, and self-supervised models in both binary and multi-class remote sensing semantic segmentation scenarios. The results demonstrate that our proposed IDGBR framework exhibits stable boundary optimization capabilities and can consistently refine boundaries of coarse segmentation results generated by different baseline models. We also discuss the crucial roles of conditional guidance and cubic timestep sampling techniques in integrating the advantages of discriminative and generative approaches. Furthermore, we categorize IDGBR’s performance under different completeness levels of coarse segmentation guidance into three levels and systematically discuss the method’s applicability and limitations. Subsequently, experiments validate the effectiveness of regularization techniques in accelerating convergence. Finally, we investigate the stability of our method’s boundary optimization under different boundary tolerance thresholds.

Future work can explore two primary directions. First, conditional diffusion models rely on multi-step iterative sampling during inference. While this strategy significantly improves segmentation quality, it also introduces additional computational overhead and inference latency. Therefore, developing more efficient sampling strategies while preserving segmentation accuracy remains a critical challenge. Second, the optimization performance of our method in some scenarios relies on the completeness of prompt information. Future research could further explore the synergistic effects of multi-granularity spatial prompts and language guidance in the optimization process to improve optimization robustness and segmentation accuracy in complex scenarios.

ACKNOWLEDGMENTS

This work was supported by the National Natural Science Foundation of China (Grants No. 42171376 and No. 42471419) and the High-Level Talent Introduction Project of Inner Mongolia University (Grant No. 10000-A25206020).

REFERENCES

- [1] K. Nogueira, M. Dalla Mura, J. Chanussot, W. R. Schwartz, and J. A. dos Santos, “Dynamic Multicontext Segmentation of Remote Sensing Images Based on Convolutional Networks,” *IEEE Trans. Geosci. Remote Sens.*, vol. 57, no. 10, pp. 7503–7520, 2019.
- [2] C. Zhang, W. Jiang, Y. Zhang, W. Wang, Q. Zhao, and C. Wang, “Transformer and CNN Hybrid Deep Neural Network for Semantic Segmentation of Very-High-Resolution Remote Sensing Imagery,” *IEEE Trans. Geosci. Remote Sens.*, vol. 60, pp. 1–20, 2022.

- [3] L. Ding, J. Zhang, and L. Bruzzone, "Semantic Segmentation of Large-Size VHR Remote Sensing Images Using a Two-Stage Multiscale Training Architecture," *IEEE Trans. Geosci. Remote Sens.*, vol. 58, no. 8, pp. 5367–5376, 2020.
- [4] D. Chen, J. A. Spencer, J. Mirebeau, K. Chen, M. Shu, and L. D. Cohen, "A generalized asymmetric dual-front model for active contours and image segmentation," *IEEE Trans. Image Process.*, vol. 30, pp. 5056–5071, 2021.
- [5] D. Marmanis, K. Schindler, J. D. Wegner, S. Galliani, M. Datcu, and U. Stilla, "Classification with an edge: Improving semantic image segmentation with boundary detection," *ISPRS J. Photogramm. Remote Sens.*, vol. 135, pp. 158–172, 2018.
- [6] A. Kirillov, Y. Wu, K. He, and R. B. Girshick, "Pointrend: Image segmentation as rendering," in *Proc. IEEE Conf. Comput. Vis. Pattern Recognit.*, 2020, pp. 9796–9805.
- [7] G. Bertasius, L. Torresani, S. X. Yu, and J. Shi, "Convolutional random walk networks for semantic image segmentation," in *Proc. IEEE Conf. Comput. Vis. Pattern Recognit.*, 2017, pp. 6137–6145.
- [8] H. Ding, X. Jiang, A. Q. Liu, N. Magnenat-Thalmann, and G. Wang, "Boundary-aware feature propagation for scene segmentation," in *Proc. IEEE Int. Conf. Comput. Vis.*, 2019, pp. 6818–6828.
- [9] Y. Wang, H. Zhang, Y. Hu, X. Hu, L. Chen, and S. Hu, "Geometric Boundary Guided Feature Fusion and Spatial-Semantic Context Aggregation for Semantic Segmentation of Remote Sensing Images," *IEEE Trans. Image Process.*, vol. 32, pp. 6373–6385, 2023.
- [10] D. Wu, Z. Guo, A. Li, C. Yu, C. Gao, and N. Sang, "Conditional Boundary Loss for Semantic Segmentation," *IEEE Trans. Image Process.*, vol. 32, pp. 3717–3731, 2023.
- [11] H. Wang, X. Wu, Z. Huang, and E. P. Xing, "High-frequency component helps explain the generalization of convolutional neural networks," in *Proc. IEEE Conf. Comput. Vis. Pattern Recognit.*, 2020, pp. 8681–8691.
- [12] Z. Lin, Y. Gao, and J. Sang, "Investigating and explaining the frequency bias in image classification," in *Proc. Int. Jt. Conf. Artif. Intell. (IJCAI)*, 2022, pp. 717–723.
- [13] L. Ardizzone, R. Mackowiak, C. Rother, and U. Köthe, "Training normalizing flows with the information bottleneck for competitive generative classification," in *Proc. Adv. Neural Inf. Process. Syst.*, 2020, pp. 7828–7840.
- [14] S. M. Ayyoubzadeh and X. Wu, "High frequency detail accentuation in CNN image restoration," *IEEE Trans. Image Process.*, vol. 30, pp. 8836–8846, 2021.
- [15] K. Schwarz, Y. Liao, and A. Geiger, "On the frequency bias of generative models," in *Proc. Adv. Neural Inf. Process. Syst.*, 2021, pp. 18126–18136.
- [16] R. Rombach, A. Blattmann, D. Lorenz, P. Esser, and B. Ommer, "High-resolution image synthesis with latent diffusion models," in *Proc. IEEE Conf. Comput. Vis. Pattern Recognit.*, 2022, pp. 10674–10685.
- [17] J. Song, C. Meng, and S. Ermon, "Denoising diffusion implicit models," in *Proc. Int. Conf. Learn. Representations*, 2021.
- [18] J. Ho, A. Jain, and P. Abbeel, "Denoising diffusion probabilistic models," in *Proc. Adv. Neural Inf. Process. Syst.*, 2020.
- [19] C. Si, Z. Huang, Y. Jiang, and Z. Liu, "Freeu: Free lunch in diffusion u-net," in *Proc. IEEE Conf. Comput. Vis. Pattern Recognit.*, 2024, pp. 4733–4743.
- [20] S. Yu, S. Kwak, H. Jang, J. Jeong, J. Huang, J. Shin, and S. Xie, "Representation alignment for generation: Training diffusion transformers is easier than you think," in *Proc. Int. Conf. Learn. Representations.*, 2025.
- [21] Z. Su, J. Zhang, L. Wang, H. Zhang, Z. Liu, M. Pietikäinen, and L. Liu, "Lightweight pixel difference networks for efficient visual representation learning," *IEEE Trans. Pattern Anal. Mach. Intell.*, vol. 45, no. 12, pp. 14956–14974, 2023.
- [22] X. Li, F. Xu, F. Liu, Y. Tong, X. Lyu, and J. Zhou, "Semantic Segmentation of Remote Sensing Images by Interactive Representation Refinement and Geometric Prior-Guided Inference," *IEEE Trans. Geosci. Remote Sens.*, vol. 62, pp. 1–18, 2024.
- [23] Y. Qiao, B. Zhong, B. Du, H. Cai, J. Jiang, Q. Liu, A. Yang, J. Wu, and X. Wang, "SAM Enhanced Semantic Segmentation for Remote Sensing Imagery Without Additional Training," *IEEE Trans. Geosci. Remote Sens.*, vol. 63, pp. 1–16, 2025.
- [24] H. Wu, Z. Du, D. Zhong, Y. Wang, and C. Tao, "FSVLM: A Vision-Language Model for Remote Sensing Farmland Segmentation," *IEEE Trans. Geosci. Remote Sens.*, vol. 63, pp. 1–13, 2025.
- [25] X. He, Y. Zhou, J. Zhao, D. Zhang, R. Yao, and Y. Xue, "Swin Transformer Embedding UNet for Remote Sensing Image Semantic Segmentation," *IEEE Trans. Geosci. Remote Sens.*, vol. 60, pp. 1–15, 2022.
- [26] M. Kampffmeyer, A. Salberg, and R. Jenssen, "Semantic segmentation of small objects and modeling of uncertainty in urban remote sensing images using deep convolutional neural networks," in *Proc. IEEE Conf. Comput. Vis. Pattern Recognit. Workshops (CVPRW)*, 2016, pp. 680–688.
- [27] W. Huang, F. Deng, H. Liu, M. Ding, and Q. Yao, "Multiscale Semantic Segmentation of Remote Sensing Images Based on Edge Optimization," *IEEE Trans. Geosci. Remote Sens.*, vol. 63, pp. 1–13, 2025.
- [28] R. Hamaguchi, A. Fujita, K. Nemoto, T. Imaizumi, and S. Hikosaka, "Effective use of dilated convolutions for segmenting small object instances in remote sensing imagery," in *Proc. IEEE/CVF Winter Conf. Appl. Comput. Vis.*, 2018.
- [29] Y. Li, X. Li, Y. Dai, Q. Hou, L. Liu, Y. Liu, M. Cheng, and J. Yang, "Lsknet: A foundation lightweight backbone for remote sensing," *Int. J. Comput. Vis.*, vol. 133, no. 3, pp. 1410–1431, 2025.
- [30] X. Chen, Z. Li, J. Jiang, Z. Han, S. Deng, Z. Li, T. Fang, H. Huo, Q. Li, and M. Liu, "Adaptive effective receptive field convolution for semantic segmentation of VHR remote sensing images," *IEEE Trans. Geosci. Remote Sens.*, vol. 59, no. 4, pp. 3532–3546, 2021.
- [31] A. Vaswani, N. Shazeer, N. Parmar, J. Uszkoreit, L. Jones, A. N. Gomez, L. Kaiser, and I. Polosukhin, "Attention is all you need," in *Proc. Adv. Neural Inf. Process. Syst.*, 2017, pp. 5998–6008.
- [32] S. Zheng, J. Lu, H. Zhao, X. Zhu, Z. Luo, Y. Wang, Y. Fu, J. Feng, T. Xiang, P. H. S. Torr, and L. Zhang, "Rethinking semantic segmentation from a sequence-to-sequence perspective with transformers," in *Proc. IEEE Conf. Comput. Vis. Pattern Recognit.*, 2021, pp. 6881–6890.
- [33] R. Strudel, R. Garcia, I. Laptev, and C. Schmid, "Segmenter: Transformer for semantic segmentation," in *Proc. IEEE Int. Conf. Comput. Vis.*, 2021, pp. 7242–7252.
- [34] L. Wang, R. Li, C. Zhang, S. Fang, C. Duan, X. Meng, and P. M. Atkinson, "UNetFormer: A UNet-like transformer for efficient semantic segmentation of remote sensing urban scene imagery," *ISPRS J. Photogramm. Remote Sens.*, vol. 190, pp. 196–214, 2022.
- [35] F. Zhang, A. Panahi, and G. Gao, "FsaNet: Frequency Self-Attention for Semantic Segmentation," *IEEE Trans. Image Process.*, vol. 32, pp. 4757–4772, 2023.
- [36] S. Borse, Y. Wang, Y. Zhang, and F. Porikli, "Inverseform: A loss function for structured boundary-aware segmentation," in *Proc. IEEE Conf. Comput. Vis. Pattern Recognit.*, 2021, pp. 5901–5911.
- [37] C. Wang, Y. Zhang, M. Cui, P. Ren, Y. Yang, X. Xie, X. Hua, H. Bao, and W. Xu, "Active boundary loss for semantic segmentation," in *Proc. AAAI Conf. Artif. Intell.*, 2022, pp. 2397–2405.
- [38] S. N. Rai, F. Cermelli, B. Caputo, and C. Masone, "Mask2anomaly: Mask transformer for universal open-set segmentation," *IEEE Trans. Pattern Anal. Mach. Intell.*, vol. 46, no. 12, pp. 9286–9302, 2024.
- [39] M. Yin, Z. Yao, Y. Cao, X. Li, Z. Zhang, S. Lin, and H. Hu, "Disentangled non-local neural networks," in *Proc. Eur. Conf. Comput. Vis.*, ser. Lecture Notes in Computer Science, vol. 12360, 2020, pp. 191–207.
- [40] L. Ding, H. Tang, and L. Bruzzone, "LANet: Local Attention Embedding to Improve the Semantic Segmentation of Remote Sensing Images," *IEEE Trans. Geosci. Remote Sens.*, vol. 59, no. 1, pp. 426–435, 2021.
- [41] C. Zheng, J. Nie, Z. Wang, N. Song, J. Wang, and Z. Wei, "High-Order Semantic Decoupling Network for Remote Sensing Image Semantic Segmentation," *IEEE Trans. Geosci. Remote Sens.*, vol. 61, pp. 1–15, 2023.
- [42] X. Li, F. Xu, A. Yu, X. Lyu, H. Gao, and J. Zhou, "A Frequency Decoupling Network for Semantic Segmentation of Remote Sensing Images," *IEEE Trans. Geosci. Remote Sens.*, vol. 63, pp. 1–21, 2025.
- [43] A. Toker, M. Eisenberger, D. Cremers, and L. Leal-Taixé, "Satsynth: Augmenting image-mask pairs through diffusion models for aerial semantic segmentation," in *Proc. IEEE Conf. Comput. Vis. Pattern Recognit.*, 2024, pp. 27685–27695.
- [44] J. Tian, L. Aggarwal, A. Colaco, Z. Kira, and M. González-Franco, "Diffuse, attend, and segment: Unsupervised zero-shot segmentation using stable diffusion," in *Proc. IEEE Conf. Comput. Vis. Pattern Recognit.*, 2024, pp. 3554–3563.
- [45] M. Zhu, Y. Liu, Z. Luo, C. Jing, H. Chen, G. Xu, X. Wang, and C. Shen, "Unleashing the potential of the diffusion model in few-shot semantic segmentation," in *Proc. Adv. Neural Inf. Process. Syst.*, 2024.
- [46] D. Baranchuk, A. Voynov, I. Rubachev, V. Khurlov, and A. Babenko, "Label-efficient semantic segmentation with diffusion models," in *Proc. Int. Conf. Learn. Representations*, 2022.
- [47] J. Wolleb, R. Sandkühler, F. Bieder, P. Valmaggia, and P. C. Cattin, "Diffusion models for implicit image segmentation ensembles," in *Proc. Int. Conf. Med. Imaging Deep Learn. (MIDL)*, vol. 172, 2022, pp. 1336–1348.

- [48] T. Amit, E. Nachmani, T. Shaharabany, and L. Wolf, “Segdiff: Image segmentation with diffusion probabilistic models,” 2021, *arXiv:2112.00390*.
- [49] W. Zhao, Y. Rao, Z. Liu, B. Liu, J. Zhou, and J. Lu, “Unleashing text-to-image diffusion models for visual perception,” in *Proc. IEEE Int. Conf. Comput. Vis.*, 2023, pp. 5706–5716.
- [50] W. Wu, Y. Zhao, M. Z. Shou, H. Zhou, and C. Shen, “Diffmask: Synthesizing images with pixel-level annotations for semantic segmentation using diffusion models,” in *Proc. IEEE Int. Conf. Comput. Vis.*, 2023, pp. 1206–1217.
- [51] Z. Li, Q. Zhou, X. Zhang, Y. Zhang, Y. Wang, and W. Xie, “Open-vocabulary object segmentation with diffusion models,” in *Proc. IEEE Int. Conf. Comput. Vis.*, 2023, pp. 7633–7642.
- [52] Y. Ji, Z. Chen, E. Xie, L. Hong, X. Liu, Z. Liu, T. Lu, Z. Li, and P. Luo, “DDP: diffusion model for dense visual prediction,” in *Proc. IEEE Int. Conf. Comput. Vis.*, 2023, pp. 21 684–21 695.
- [53] T. Chen, L. Li, S. Saxena, G. E. Hinton, and D. J. Fleet, “A generalist framework for panoptic segmentation of images and videos,” in *Proc. IEEE Int. Conf. Comput. Vis.*, 2023, pp. 909–919.
- [54] S. Lee, S. Jung, and H. Seo, “Spectrum translation for refinement of image generation (STIG) based on contrastive learning and spectral filter profile,” in *Proc. AAAI Conf. Artif. Intell.*, 2024, pp. 2929–2937.
- [55] X. Yang, D. Zhou, J. Feng, and X. Wang, “Diffusion probabilistic model made slim,” in *Proc. IEEE Conf. Comput. Vis. Pattern Recognit.*, 2023, pp. 22 552–22 562.
- [56] D. J. Field, “Relations between the statistics of natural images and the response properties of cortical cells,” *JOSA Vol. 4 Issue 12 pp.* 2379–2394, 1987.
- [57] J. Gao, C. Xiao, L. M. Glass, and J. Sun, “COMPOSE: cross-modal pseudo-siamese network for patient trial matching,” in *Proc. ACM SIGKDD Int. Conf. Knowl. Discov. Data Min.*, 2020, pp. 803–812.
- [58] J. Yao, B. Yang, and X. Wang, “Reconstruction vs. Generation: Taming Optimization Dilemma in Latent Diffusion Models,” 2025.
- [59] H. Zheng, W. Nie, A. Vahdat, and A. Anandkumar, “Fast training of diffusion models with masked transformers,” *Trans. Mach. Learn. Res.*, vol. 2024, 2024.
- [60] S. Gao, P. Zhou, M. Cheng, and S. Yan, “Masked diffusion transformer is a strong image synthesizer,” in *Proc. IEEE Int. Conf. Comput. Vis.*, 2023, pp. 23 107–23 116.
- [61] M. Oquab, T. Darcet, T. Moutakanni, H. V. Vo, M. Szafraniec, V. Khalidov, P. Fernandez, D. Haziza, F. Massa, A. El-Nouby, M. Assran, N. Ballas, W. Galuba, R. Howes, P. Huang, S. Li, I. Misra, M. Rabbat, V. Sharma, G. Synnaeve, H. Xu, H. Jégou, J. Mairal, P. Labatut, A. Joulin, and P. Bojanowski, “Dinov2: Learning robust visual features without supervision,” *Trans. Mach. Learn. Res.*, vol. 2024, 2024.
- [62] C. Mou, X. Wang, L. Xie, Y. Wu, J. Zhang, Z. Qi, and Y. Shan, “T2i-adapter: Learning adapters to dig out more controllable ability for text-to-image diffusion models,” in *Proc. AAAI Conf. Artif. Intell.*, 2024, pp. 4296–4304.
- [63] Q. Zhu, Y. Zhang, L. Wang, Y. Zhong, Q. Guan, X. Lu, L. Zhang, and D. Li, “A Global Context-aware and Batch-independent Network for road extraction from VHR satellite imagery,” *ISPRS J. Photogramm. Remote Sens.*, vol. 175, pp. 353–365, 2021.
- [64] J. Li, Y. Wei, T. Wei, and W. He, “A Comprehensive Deep-Learning Framework for Fine-Grained Farmland Mapping From High-Resolution Images,” *IEEE Trans. Geosci. Remote Sens.*, vol. 63, pp. 1–15, 2025.
- [65] S. Ji, S. Wei, and M. Lu, “Fully Convolutional Networks for Multisource Building Extraction From an Open Aerial and Satellite Imagery Data Set,” *IEEE Trans. Geosci. Remote Sens.*, vol. 57, no. 1, pp. 574–586, 2019.
- [66] Photogrammetry, T.I.S., (ISPRS), R.S., “2d semantic labeling contest - potsdam,” [Online]. Available: <https://www.isprs.org/resources/datasets/benchmarks/UrbanSemLab/2d-sem-label-potsdam.aspx>, 2022.
- [67] ISPRS, “2d semantic labeling - vaihingen,” [Online]. Available: <https://www.isprs.org/resources/datasets/benchmarks/UrbanSemLab/2d-sem-label-vaihingen.aspx>, 2022.
- [68] L. Chen, Y. Zhu, G. Papandreou, F. Schroff, and H. Adam, “Encoder-decoder with atrous separable convolution for semantic image segmentation,” in *Proc. Eur. Conf. Comput. Vis.*, 2018, pp. 833–851.
- [69] E. Xie, W. Wang, Z. Yu, A. Anandkumar, J. M. Álvarez, and P. Luo, “Segformer: Simple and efficient design for semantic segmentation with transformers,” in *Proc. Adv. Neural Inf. Process. Syst.*, 2021, pp. 12 077–12 090.
- [70] R. Margolin, L. Zelnik-Manor, and A. Tal, “How to evaluate foreground maps,” in *Proc. IEEE Conf. Comput. Vis. Pattern Recognit.*, 2014, pp. 248–255.

APPENDIX

EQUATION DERIVATION DETAILS

A. Proof of the Wiener Filter Solution in the Diffusion Probabilistic Model

Here, we present the general mathematical derivation for treating the diffusion model as a Wiener filter. Assume that z_0 is a wide-sense stationary signal and ϵ is white Gaussian noise with variance $\sigma^2 = 1$. In the Diffusion Probabilistic Model (DPM), the signal and noise are mixed at any arbitrary timestep t , and the resulting observation can be expressed as: $z_t = \sqrt{\bar{\alpha}_t} z_0 + \sqrt{1 - \bar{\alpha}_t} \epsilon$. To further simplify the model and obtain an explicit closed-form solution, we introduce a linear denoising Wiener filter h_t . The objective function for the diffusion model can then be redefined as

$$J_t = \|\sqrt{\bar{\alpha}_t} z_0 - h_t * z_t\|^2 \quad (\text{A1})$$

where $\bar{\alpha}_t$ denotes the scaling factor for the signal component at timestep t , which decreases as t increases; the symbol “*” denotes the convolution operator.

To facilitate analysis and derive the optimal solution for the filter, we convert the above time-domain convolution operation into the frequency domain. According to the convolution theorem, the time-domain convolution $h_t * z_t$ is equivalent to the product in the frequency domain, i.e., $\mathcal{F}[h_t * z_t] = \mathcal{F}[h_t] \cdot \mathcal{F}[z_t]$, where $\mathcal{F}[\cdot]$ denotes the Fourier transform and \mathcal{H}_t represents the corresponding filter in the frequency domain. Thus, the transition from the time-domain convolution to frequency-domain multiplication can be expressed as:

$$\mathcal{H}_t (\sqrt{\bar{\alpha}_t} z_0 + \sqrt{1 - \bar{\alpha}_t} \mathcal{F}[\epsilon]) = \mathcal{F} [h_t * (\sqrt{\bar{\alpha}_t} z_0 + \sqrt{1 - \bar{\alpha}_t} \epsilon)] \quad (\text{A2})$$

Furthermore, the error signal $J_t(f)$ can be written as

$$\mathcal{J}_t(f) = \sqrt{\bar{\alpha}_t} \mathcal{Z}_0 - \mathcal{H}_t (\sqrt{\bar{\alpha}_t} \mathcal{Z}_0 + \sqrt{1 - \bar{\alpha}_t} \mathcal{F}[\epsilon]) \quad (\text{A3})$$

We obtain the filter by minimizing the mean squared error objective:

$$\begin{aligned} \min_h \mathbb{E} [\|\mathcal{J}_t(f)\|_2^2] &= \min_h \mathbb{E} [\mathcal{J}_t(f)^* \mathcal{J}_t(f)] \\ &= \min_h \mathbb{E} [(\sqrt{\bar{\alpha}_t} \mathcal{Z}_0 - \mathcal{H}_t (\sqrt{\bar{\alpha}_t} \mathcal{Z}_0 + \sqrt{1 - \bar{\alpha}_t} \mathcal{F}[\epsilon])) \cdot (\sqrt{\bar{\alpha}_t} \mathcal{Z}_0 - \mathcal{H}_t (\sqrt{\bar{\alpha}_t} \mathcal{Z}_0 + \sqrt{1 - \bar{\alpha}_t} \mathcal{F}[\epsilon]))] \end{aligned} \quad (\text{A4})$$

where the symbol $*$ denotes the complex conjugate. To obtain the Wiener filter that minimizes the mean squared error, we take the derivative of the objective function with respect to $\mathcal{H}_t(f)$ and set it to zero. Since ϵ and z_0 are conditionally independent, we have:

$$\begin{aligned} \frac{\partial \mathbb{E} [\|\mathcal{J}_t(f)\|_2^2]}{\partial \mathcal{H}_t(f)} &= 2\mathcal{H}_t (\bar{\alpha}_t |\mathcal{Z}_0(f)|^2 + (1 - \bar{\alpha}_t) |\mathcal{F}[\epsilon]|^2) \\ &\quad - 2\bar{\alpha}_t |\mathcal{Z}_0(f)|^2 = 0 \end{aligned} \quad (\text{A5})$$

where $|\mathcal{Z}_0(f)|^2 = \mathbb{E}[\mathcal{Z}_0 \mathcal{Z}_0^*]$, $|\mathcal{F}[\epsilon]|^2 = \mathbb{E}[\mathcal{F}[\epsilon] \mathcal{F}[\epsilon]^*]$. Since the variance of the white noise is σ^2 , $|\mathcal{F}[\epsilon]|^2$ is a constant σ^2 . Simplifying further, we obtain:

$$\mathcal{H}_t^*(f) = \frac{\bar{\alpha}_t |\mathcal{Z}_0(f)|^2}{\bar{\alpha}_t |\mathcal{Z}_0(f)|^2 + (1 - \bar{\alpha}_t) \sigma^2} \quad (\text{A6})$$

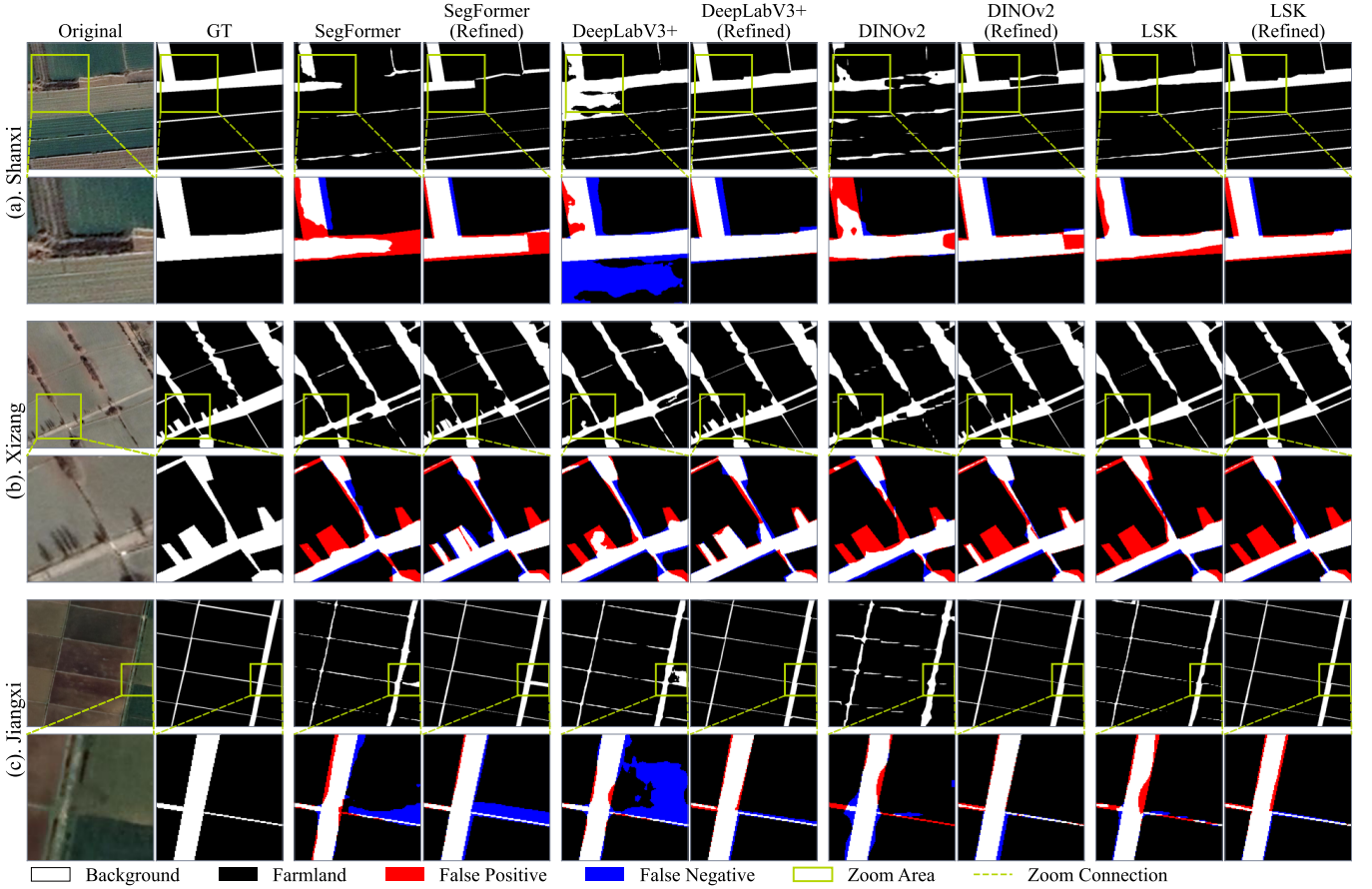


Fig. B1: Qualitative results of different methods on FGFD.

Here, $|\mathcal{Z}_0(f)|^2$ denotes the power spectrum of z_0 , and $\mathcal{H}_t(f)$ denotes the frequency response of h_t . According to the commonly assumed power-law distribution of natural image spectra [56], we have $\mathbb{E}[|\mathcal{Z}_0(f)|^2] \approx 1/f^2$. Thus, the Wiener filter in the frequency domain can be expressed as:

$$\mathcal{H}_t^*(f) \approx \frac{\bar{\alpha}_t}{\bar{\alpha}_t + (1 - \bar{\alpha}_t)f^2} \quad (\text{A7})$$

EXPERIMENTAL DETAILS

A. Qualitative Results on FGFD

FGFD is primarily used to validate the boundary optimization capability of the IDGBR framework in complex texture scenes.

The complex spatiotemporal attributes of farmland pose significant challenges to traditional discriminative models for segmentation. As shown in Fig. B1, the visualization results collectively demonstrate the distinguishability of farmland and the continuity of field roads in three farmland scenarios. Fig. B1 (a) shows typical northern dryland farmland in Shanxi. For non-cultivated areas that are difficult to distinguish, even when patches appear regular in the original imagery, discriminative models produce patches with incomplete geometric structures and fragmented boundaries. Our method effectively suppresses low-confidence artifact regions, significantly improving patch boundary integrity and standardization. Fig. B1

(b) depicts highland grassland in Tibet. In the original imagery, shadows cast by trees along farmland boundaries create light-dark divisions within the plots. Discriminative models are prone to boundary misclassification errors in such areas. Our method mitigates segmentation errors of baseline models in shadow regions, enhancing the accuracy and continuity of farmland boundary recognition. Fig. B1 (c) showcases composite farmland in Jiangxi, where farmland boundaries are often obscured by dense vegetation cover, resulting in blurred boundaries. Due to the minimal spectral differences between vegetation and farmland in the original image, discriminative models struggle to accurately delineate boundary positions, leading to boundary ambiguity and discontinuous segmentation. Our method corrects boundary blurring caused by vegetation interference, improving the geometric consistency and completeness of segmentation results in complex regions.

B. Qualitative Results of the WHU Building Dataset

To validate the effectiveness of IDGBR in building boundary extraction and cross-temporal generalization, we conducted experiments on the bi-temporal images of the WHU Building Change Detection dataset.

Figs. B2 and B3 demonstrate the qualitative optimization results of IDGBR on post-disaster and post-reconstruction phase images from the WHU Building dataset, respectively. It can be observed that the original discriminative models

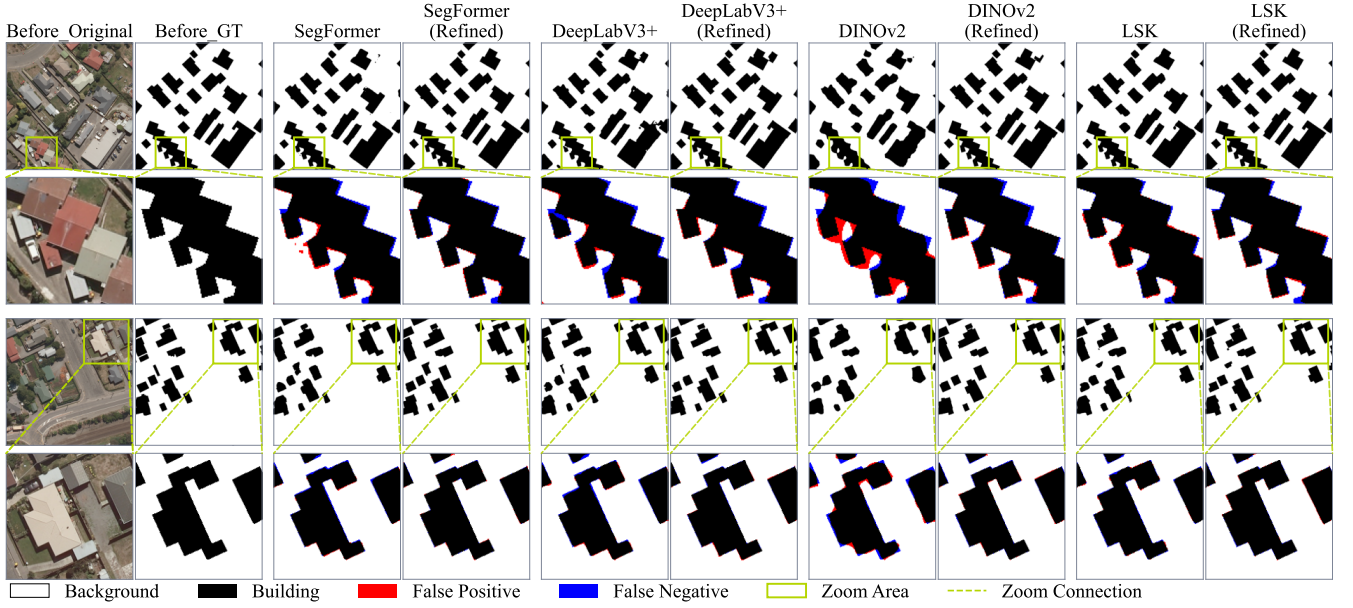


Fig. B2: Qualitative analysis on the WHU Building post-disaster phase dataset.

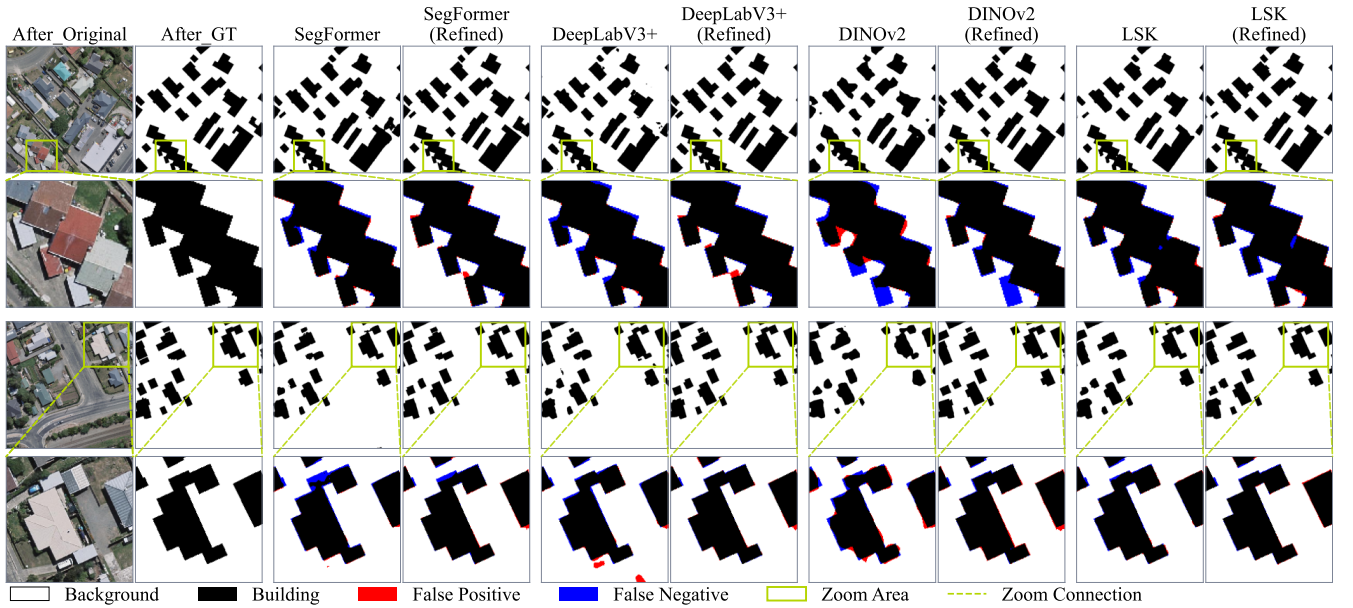


Fig. B3: Qualitative analysis on the WHU Building post-reconstruction phase dataset.

generally exhibit significant errors near building boundaries, including local false responses, irregular boundary contours, and insufficient geometric structural integrity, particularly in areas with complex roof shapes or blurred boundaries. After introducing IDGBR, all models show significantly reduced errors at boundaries, with smoother and more coherent building edges, and well-preserved detailed morphology, demonstrating the method's clear advantages in boundary modeling. Furthermore, the cross-temporal transfer experiments in Fig. B3 verify that models optimized with IDGBR maintain high boundary accuracy during the reconstruction phase, significantly suppressing segmentation errors caused by cross-temporal differences while maintaining stable boundary morphology. This

indicates that IDGBR possesses strong temporal stability and cross-scene adaptation capabilities.